GlueX-doc-1004-v5

Track Finding and Fitting in GlueX: Development Report IV

David Lawrence
Simon Taylor

Jefferson Lab

March 21, 2008

Abstract

Progress on simulation and reconstruction of charged particle tracking for the GlueX detector is presented. Significant work has been done on track finding and the geometry has been updated to reflect changes in the detector design that are to be presented during the CD-3 review. Resolutions obtained using the new geometry are presented.

Contents

1 Introduction

Charged particle tracking in the GlueX detector (Figure 1) in Hall-D primarily involves two detector systems: The Central Drift Chambers (CDC) and the Forward Drift chambers (FDC). The expected performance (resolutions and pattern recognition) of the whole tracking system is currently being studied using a detailed simulation package based on *GEANT*. The Hall-D simulation package also includes a complete set of generators that allow for study of events that include both EM background and signal based on realistic phase space distributions. Reconstruction code has also been developed that is capable of full event reconstruction using only hit information that will be available in the real data stream. Figure 2 shows the Hall-D Event Viewer with a 5-track event.

This document updates the progress in tracking simulation and reconstruction for the GlueX detector in Hall-D. It focuses on work that has been done since the last tracking report report (Ref. [6]). Much of the recent work has focused on studying the FDC and track finding in particular. A wires-only design was studied to contrast with the nominal cathode strip design and that work is presented here. Details on the (multiple) algorithms developed for track finding are given.

Several changes to the geometry have been made since the last report [6]. These include additional layers in the CDC and a shortened length. The positions of the FDC packages were also changed to bring them all inside of the high-field region of the solenoid. Numerous other changes to the geometry were made to both reduce the material in the FDC, and include material that will be present for the infrastructure (cooling, electronics, cables ,...). These are documented in Ref. [1]. These changes affect the background rates for the chambers and TOF detectors and the tracking resolutions. Updated values for these are presented here for the new geometry and, where appropriate, compared to the

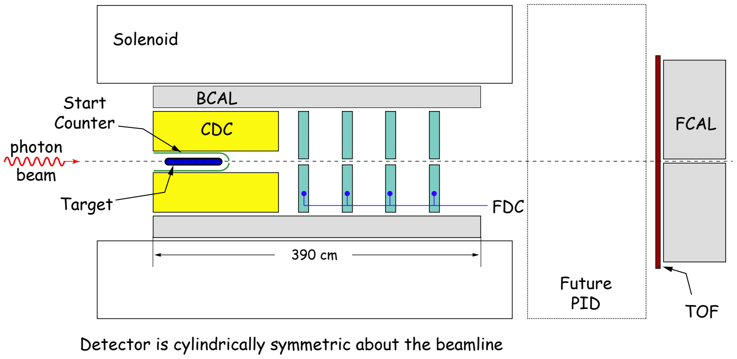

Figure 1: Diagram of the Hall-D detector indicating where the major components are.

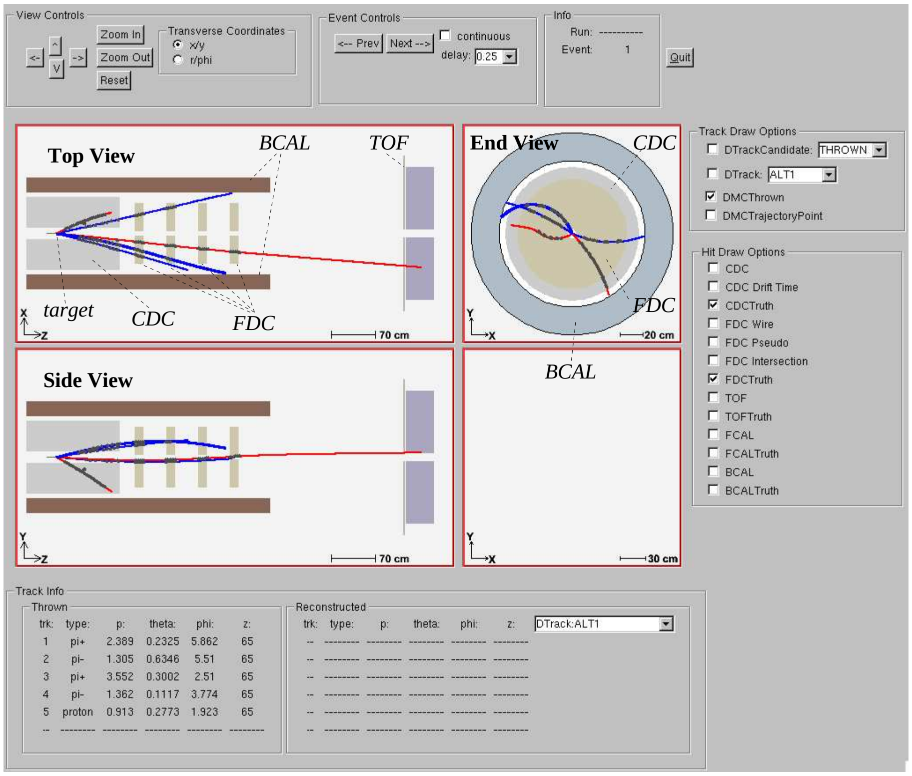

Transverse Coordinates
● x/y
○ r/phi

☐ continuous
delay: 0.25

Info
Run: ----------
Event: 1

Track Draw Options
☐ DTrackCandidate: THROWN
☐ DTrack: ALT1
☑ DMCThrown
☐ DMCTrajectoryPoint

Hit Draw Options
☐ CDC
☐ CDC Drift Time
☑ CDCTruth
☐ FDC Wire
☐ FDC Pseudo
☐ FDC Intersection
☑ FDCTruth
☐ TOF
☐ TOFTruth
☐ FCAL
☐ FCALTruth
☐ BCAL
☐ BCALTruth

Track Info

Thrown

trk:	type:	p:	theta:	phi:	z:
1	pi+	2.389	0.2325	5.862	65
2	pi-	1.305	0.6346	5.51	65
3	pi+	3.552	0.3002	2.51	65
4	pi-	1.362	0.1117	3.774	65
5	proton	0.913	0.2773	1.923	65
--	--------	--------	--------	--------	--------

Reconstructed

DTrack:ALT1

trk:	type:	p:	theta:	phi:	z:
--	--------	--------	--------	--------	--------
--	--------	--------	--------	--------	--------
--	--------	--------	--------	--------	--------
--	--------	--------	--------	--------	--------
--	--------	--------	--------	--------	--------
--	--------	--------	--------	--------	--------

Figure 2: The Hall-D single event viewer showing a 5 track event. This event was from a t-channel $\gamma p \rightarrow X(3000)p \rightarrow p2(\pi^+\pi^-)$ reaction. The red lines are negative tracks while the blue ones are positive. The thicker blue line is the proton.

March 2007 design from 1 year ago.

2 Geometry

Geometry version 4 (GeomV4) was used for the current study and is described in Ref. [1]. Figures 4 - 11 show comparisons between the simulation as defined in March 2007 and GeomV4. The major differences between these 2 geometries are listed below.

Figure 3 shows the magnetic field map with the relative locations of the CDC and FDC superimposed. Note that this is the 1500A field map as opposed to the 1400A field map used last year. The 1500A field map has a maximum value of 2.2T on the beamline while the 1400A map has a maximum of 2.0T on the beamline.

Figure 6 shows the photon reconstruction efficiency in the combined BCAL and FCAL calorimetry system (see Ref. [2]). The dip at 11^o is due to the boundary between the two calorimeters. Three geometries are shown on the plot. The *March 2007* geometry had much more material in the FDC support frames and had packages located further downstream(lower angles). The *March 2008a* and *March 2008b* geometries both have less material in the frames and had the packages position further upstream (larger angles). The

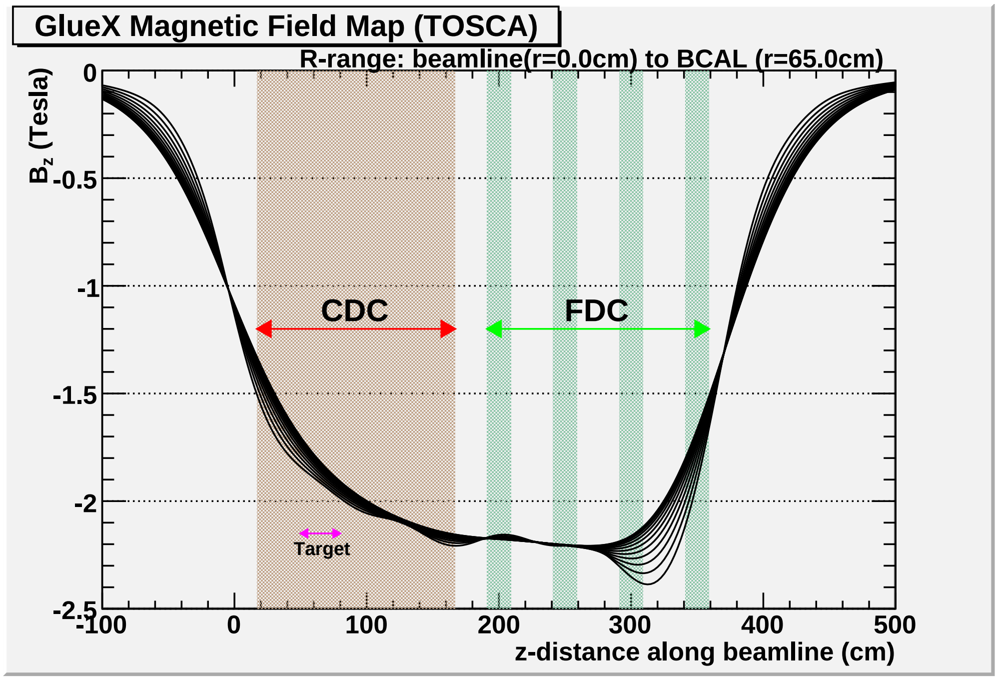

Figure 3: The z-component (along the beamline) of the magnetic field as a function of z. The locations of the CDC and FDC are marked. The multiple black lines correspond to the field at various radial distances from the beamline. Also shown is the location of the 30 cm LH_2 target, centered at $z = 65$ cm in this coordinate system. This map was derived from a TOSCA calculation with 1500A of current in the solenoid.

difference between *March 2008a* and *March 2008b* is that the FDC cables were removed in the latter. This was done to see the effect that routing the cables out the upstream end of the magnet would have as opposed to the nominal design which has them exiting through the downstream end .

Figure 7 shows the amount of material seen by a 90^0 straight track in the CDC. The two curves show the number of integrated radiation lengths for the current design(*March 2008*) and the CDC as defined in the simulation last year(*March 2007*). As noted before, the "March 2007" geometry shown here is not the design as of March 2007. Rather, it is the design that was represented in the simulation at the time which was much older. The "March 2007" curve is shown here only as a point of reference for comparing to the geometry used in the previous tracking note [6]. There are 4 main differences between these 2 geometries that can be seen in the 2 curves.

- The "March 2007" geometry had the first layer start at R=16.049cm while the March 2008 geometry has its first layer at R=10.96cm

- The "March 2007" geometry had a 2mm thick Aluminum inner skin at about R=15cm while the March 2008 geometry replaced this with only a think sheet of Aluminized Mylar at around R=9cm.

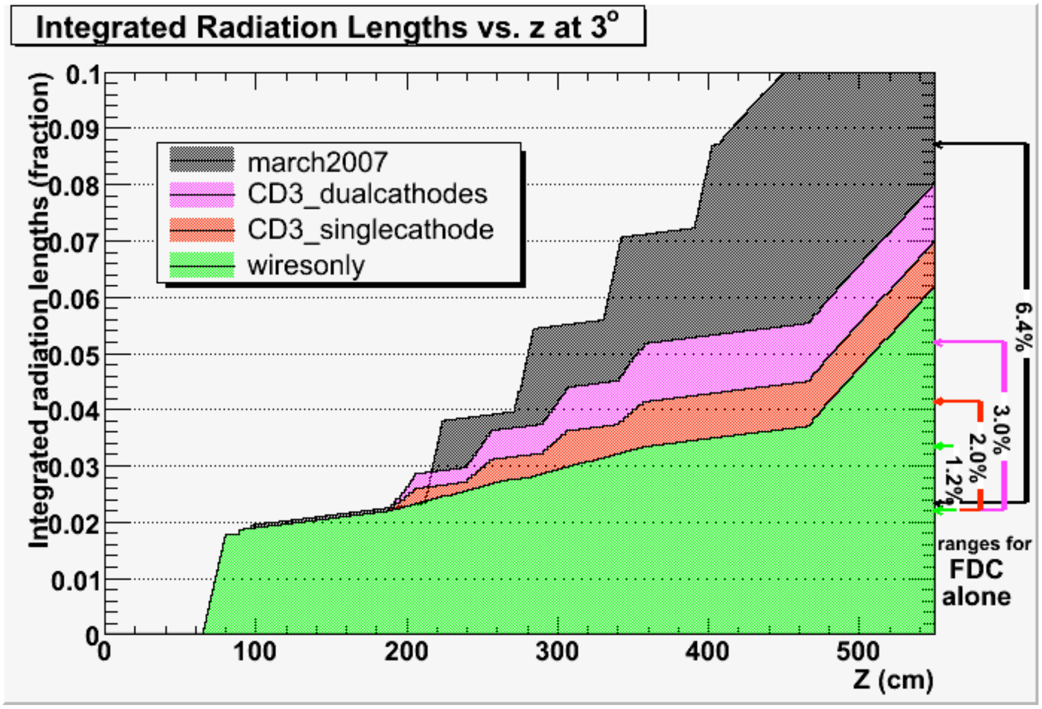

Figure 4: Integrated radiation lengths (along path) in the FDC as a function of z for a ray going from the center of the target out at $\theta = 3^o$. Four different geometries are shown. The magenta colored distribution ("CD3_dualcathodes") geometry is the current baseline geometry for CD3.

- The "March 2007" geometry had pure Kapton straw tubes while the March 2008 geometry replaced these with Aluminized Kapton straw tubes. This causes the slight increase in the overall slope of the curves between R=16cm and R=60cm.
- The "March 2007" geometry had only 23 layers of straws while the March 2008 geometry (as defined in the simulation) has 25 layers[1].

Figure 12 shows a comparison of the geometry simulated in March 2007 as compared to the current design. There are several differences between the two geometries not included in the above list. Namely:

- Material in active area of FDC reduced (see figure 4)
- Positions of FDC packages shifted upstream (i.e. to larger polar angles)

---

[1] The actual design now calls for only 24 layers to allow room for the FDC cables to be brought out through the upstream end of the solenoid. The studies presented here though, use the 25 layer design.

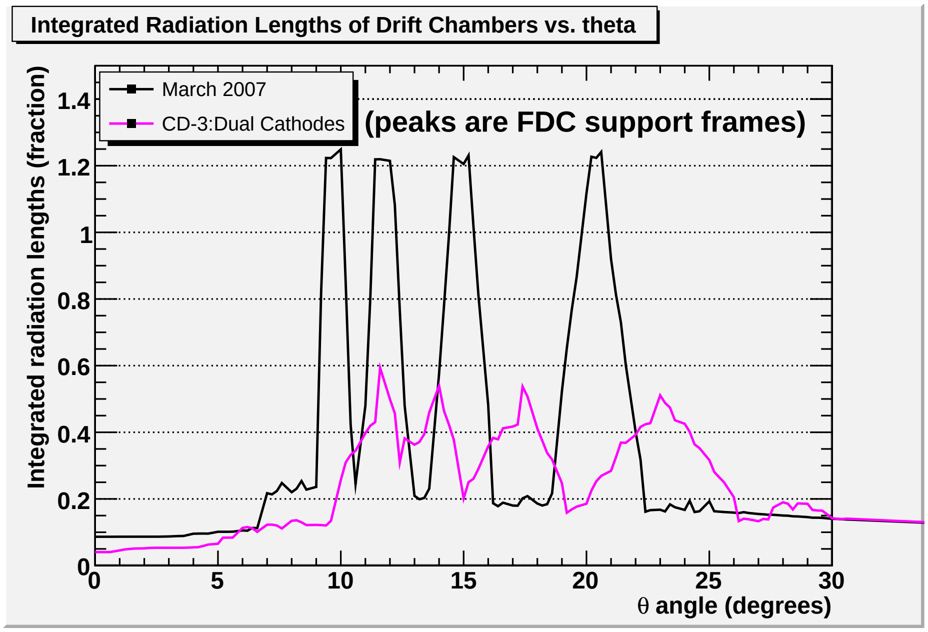

Figure 5: Integrated radiation lengths (along path) as a function of θ for rays originating at the center of the target. Both the March 2007 and current geometries are shown. The peaks correspond to the FDC support frames.

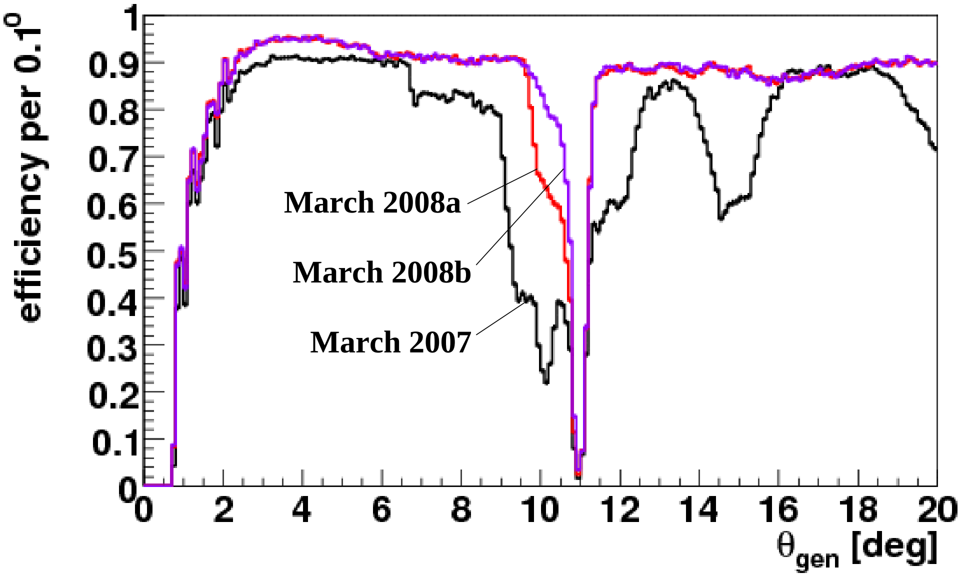

Figure 6: Photon reconstruction efficiency as a function of angle for various geometries. See the text for details.

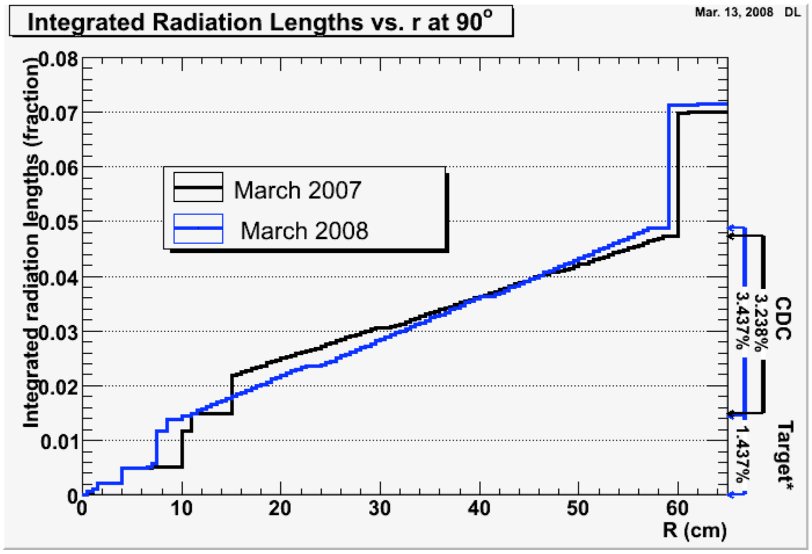

Figure 7: Integrated radiation lengths in the CDC as a function of R for a ray going from the center of the target out at $\theta = 90^o$. Note that the 1.437% value marked for the target is for the entire target package including the target, scattering chamber, and start counter. Also note that “March 2007” refers to the geometry that was in the repository at that time, which was grossly out of date with the official design. See the text for a more detailed explanation of this plot.

- CDC shortened from 175cm to 150cm

This plot clearly shows the improvements obtained by reducing the FDC material in the active region. In particular the resolution of 2GeV/c particles at 10° improved by nearly 2%. This plot also shows that by moving the FDC packages upstream, that the poorer resolution “hump” is shifted to higher polar angles. Optimization of the package positions along with the CDC length is still needed.

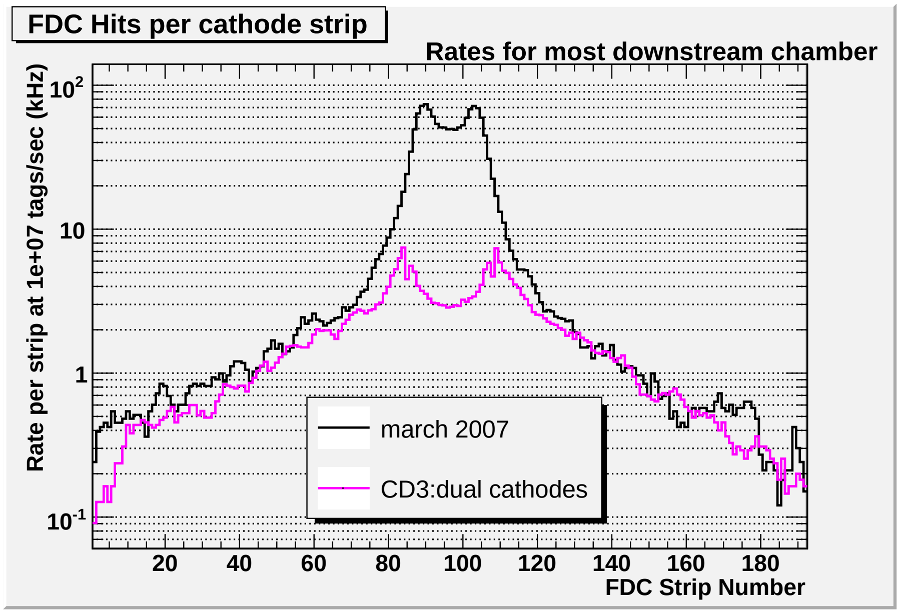

Figure 8: Rate in the FDC cathode strips due to EM background for 10^7 tagged γ/s. Both the March 2007 and current geometries are shown. Note that the central 24 strips went all the way through the beam hole in the March 2007 geometry, but for the current geometry, these were cut in half. This both removed significant material from the beamline and reduced the rate in those strips by half.

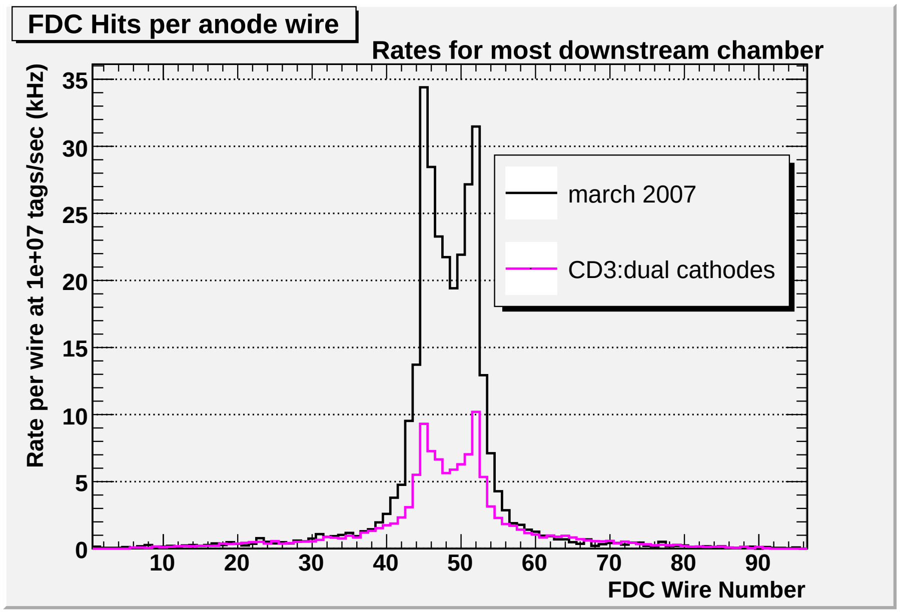

Figure 9: Rate in the FDC anode wires due to EM background for 10^7 tagged γ/s. Both the March 2007 and current geometries are shown.

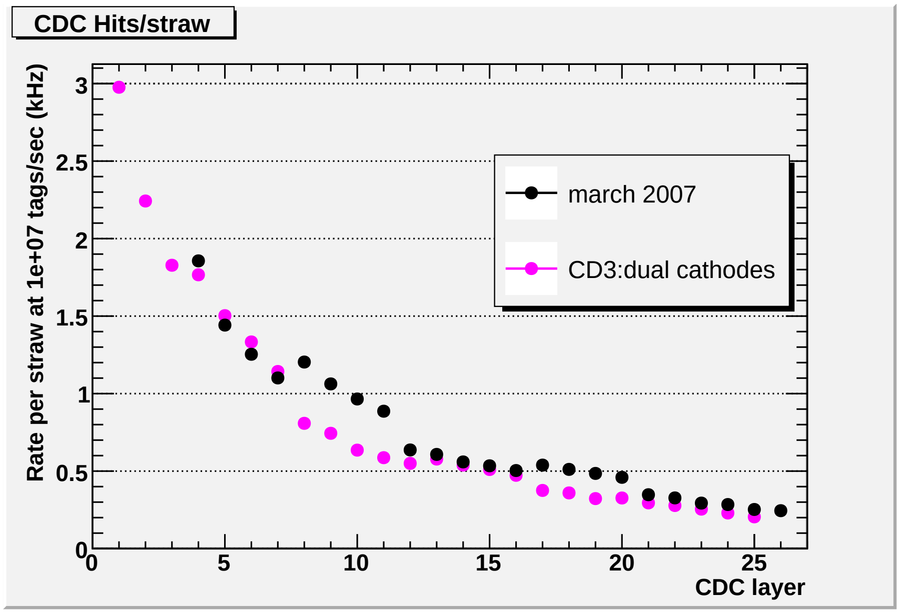

Figure 10: Rate in the CDC wires due to EM background for 10^7 tagged γ/s. Both the March 2007 and current geometries are shown. The "march 2007" points are shifted up by 3 in layer number to more fairly compare the 2 geometries since the first layer in the March 2007 design was at 16.049 cm and the 4th layer of the March 2008 design was at 16.304 cm.

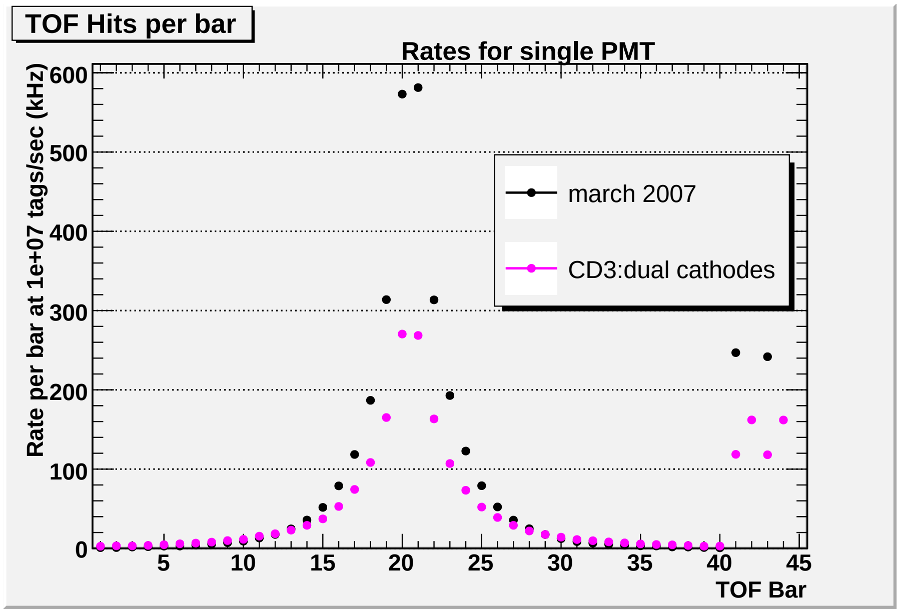

Figure 11: Rate in the TOF due to EM background for 10^7 tagged γ/s. Both the March 2007 and current geometries are shown. Bar numbers 41-44 are the half-length bars that physically are located at the center of the array. Their position on this plot is merely an artifact of the numbering scheme.

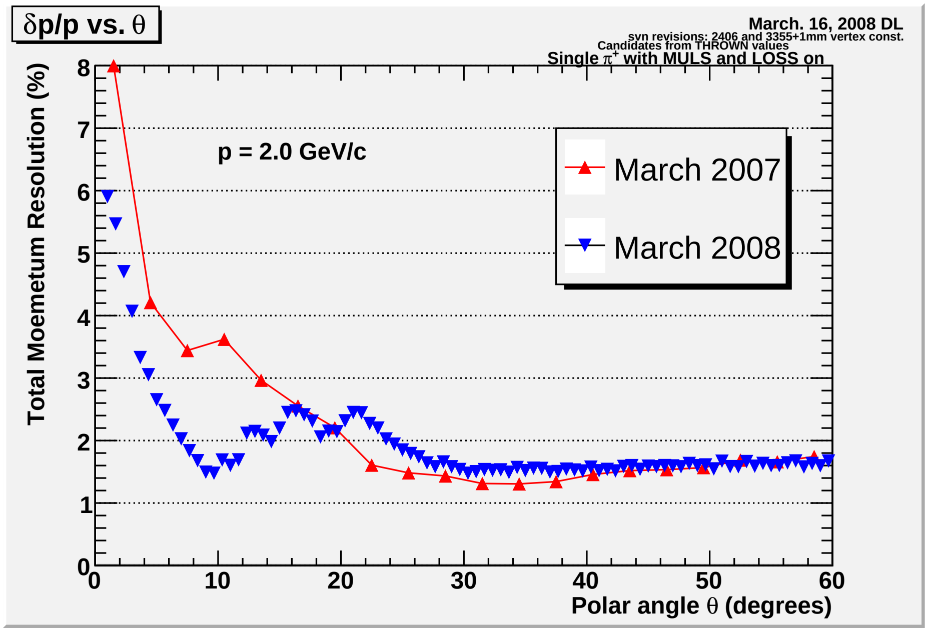

Figure 12: Comparison of total momentum resolution for the geometry simulated in March 2007 and the current geometry. See text for more details.

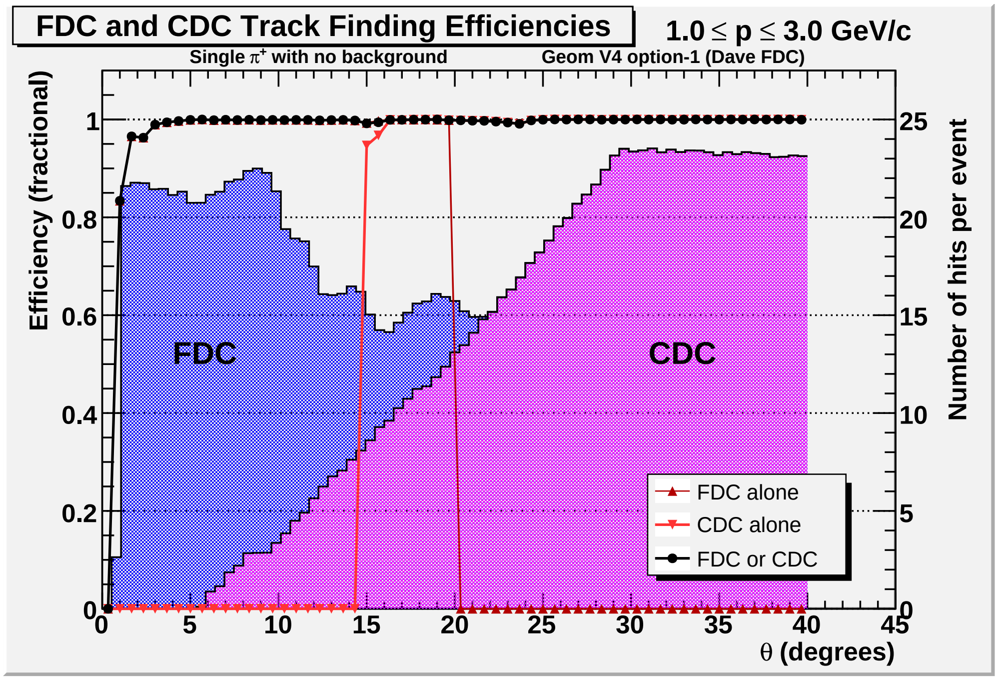

Figure 13: Track finding efficiency (left axis) and total number of tracking hits (right axis) vs. polar angle θ. The two red efficiency curves are for the individual FDC and CDC track finders. The black curve is the OR of the two. The shaded areas represent the number of wire hits in the FDC and CDC. They are plotted such that the FDC hits are added to the CDC hits so that the total, combined hits can easily be read using the right hand axis.

3 Track Finding

Track finding in the chambers has been studied using multiple algorithms. The CDC uses the seed-based algorithm described in Section 3.1. For the FDC, both a segment-based and a Hough transform algorithm were studied as described in Section 3.2. The default finder for the FDC is the segment-based one, but the Hough transform was useful in studying the wires-only design as decribed in Section 3.2.2.

One of the obvious areas of concern in the track finding would be the interface between the CDC and the FDC. There turns out to be significant enough overlap between the two detectors that this does not appear to be an issue. Figure 13 illustrates this by showing the single track finding efficiency for the CDC alone, the FDC alone, and the OR of the CDC and FDC finders . In this the plot, at least 10 hits were required in the CDC efficiency. Similarly, at least 5 hits were required in the FDC efficiency. Areas where these criteria were not met had the efficiency explicitly set to zero. The plot shows the single track finding efficiency is greater than 98% in the absence of background.

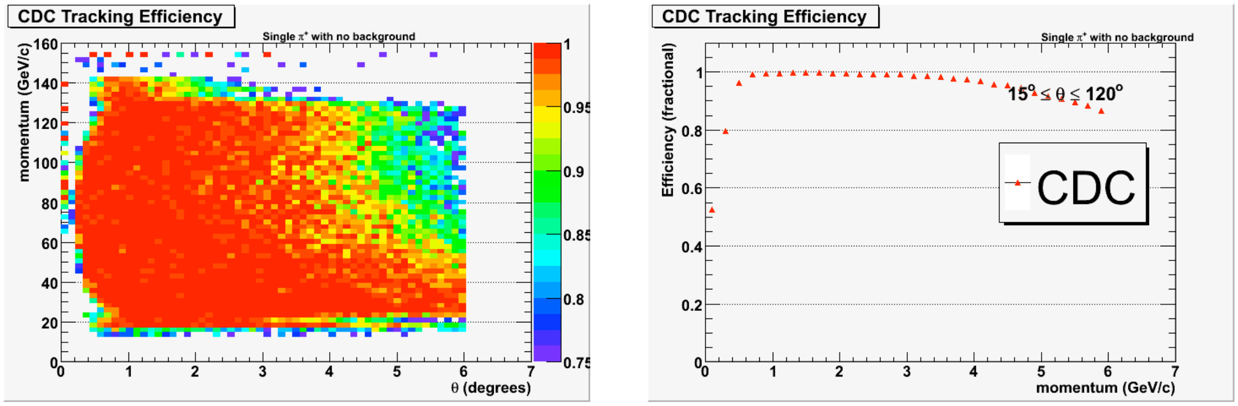

Figure 14: CDC track finding efficiencies for single π^+ events with no background. The plot on the left shows the track finding efficiency as a function of both total momentum and polar angle. (Note that the axis titles are mistakenly swapped.) The plot on the right shows the projection of the left plot onto the x-axis for tracks with $15° \leq \theta \leq 120°$.

3.1 Track Finding in the CDC

For the CDC, a seed-based track finder was developed. This finder started with axial wire hits in the X-Y plane. Starting with the outermost hit, neighboring hits were found on each layer to form clusters and clusters on neighboring layers merged to form *sub*-seeds. The sub-seeds were separated by sections with stereo wires. The sub-seeds were then linked across the stereo super-layers to form full seeds. A seed was fit to a circle and the intersection of the stereo wires with the circle was used to find the z-location of the stereo-wire hits to form full 3D space-points. The circle fit from the axial wires was used to estimate the transverse momentum and the azimuthal angle ϕ of the candidate. The 3D space points derived from the stereo wires were used to determine the polar angle θ and the z-location of the vertex (assumed to be on the beamline).

Figure 14 shows 2 plots indicating the track finding efficiency of the CDC with no background. The plot on the right in the figure indicates a loss in efficiency at low momentum. The plot on the left shows that this is due to angles outside the range of $\theta = 40°$ to $\theta = 100°$. For the low angle tracks ($\theta < 30°$), the CDC starts to lose hits due to the track exiting through the endplate.The is also a loss in efficiency for or large angles at large momentum. This is a region where the the magnetic field starts to drop off rapidly (see figure 3) and the tracks are essentially straight leaving us with no analyzing power for the momentum.

Figure 15 shows the track finding efficiency in the CDC as a function of momentum in the presence of background. The track finding efficiency in the CDC remains high and unchanged for beam intensities up to 4×10^8 tagged γ/s. The largest contributor to the overall background in the chambers is from electromagnetic interactions in the target. These, however, tend to be low multiplicity reactions whose products are very forward

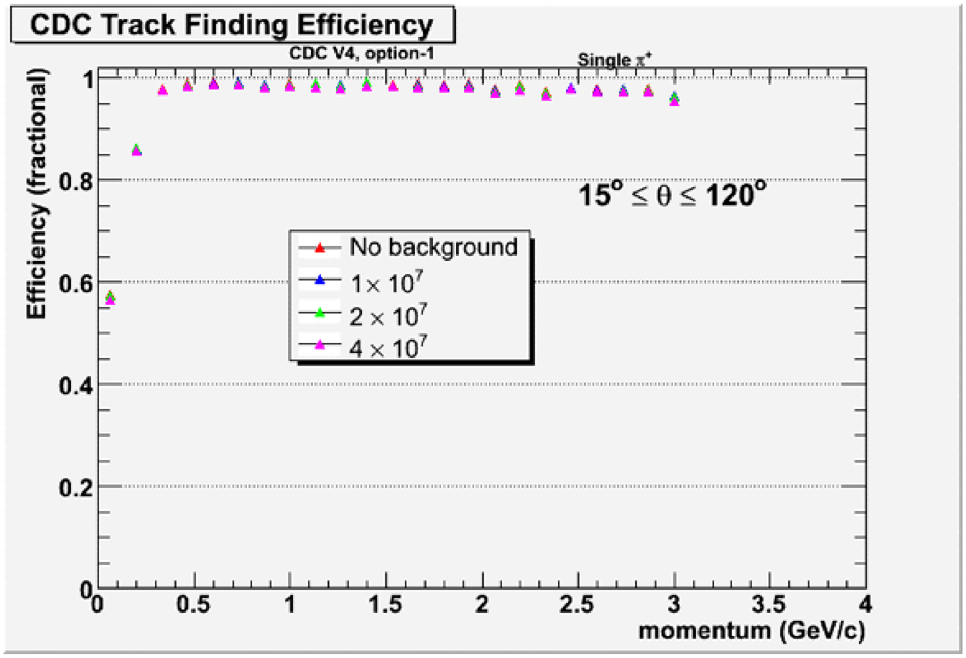

Figure 15: CDC track finding efficiency as a function of total momentum in the presence of various levels of E.M. background. The correlated E.M. background (i.e. real charged tracks) tends to be very forward biased so the effect on the CDC track finding efficiency is quite small.

biased resulting in fairly low rates in the CDC region. One can see from figures 9 and 10 that the highest rate wire in the CDC is only 1/3 that of the highest rate seen by the FDC anodes.

3.2 Track Finding in the FDC

3.2.1 Segment-Based Finder

Since the FDC packages are separated in z, it is natural to think of associating hits in individual packages into track segments from which crude track parameters can be derived. The segment-based finder forms segments by looking for nearest neighbors (within a 5 cm radius) from one wire plane to the next within a package, determines preliminary track parameters, and links segments together by swimming the track through the field from one package to the next. The linked segments then form track candidates feeding the final fitting algorithm. For details on the segment-based track finding and fitting procedure please see the Appendix.

Figure 16 shows the track-finding efficiency for single (non-decaying) pion events thrown from the center of the target. The efficiency is defined to be the ratio of events for which the number of hits matched to a candidate track swum through the field was at least 50% of the number of hits matched to a thrown track swum through the field to the number of thrown events. For both the numerator and the denominator, the mini-

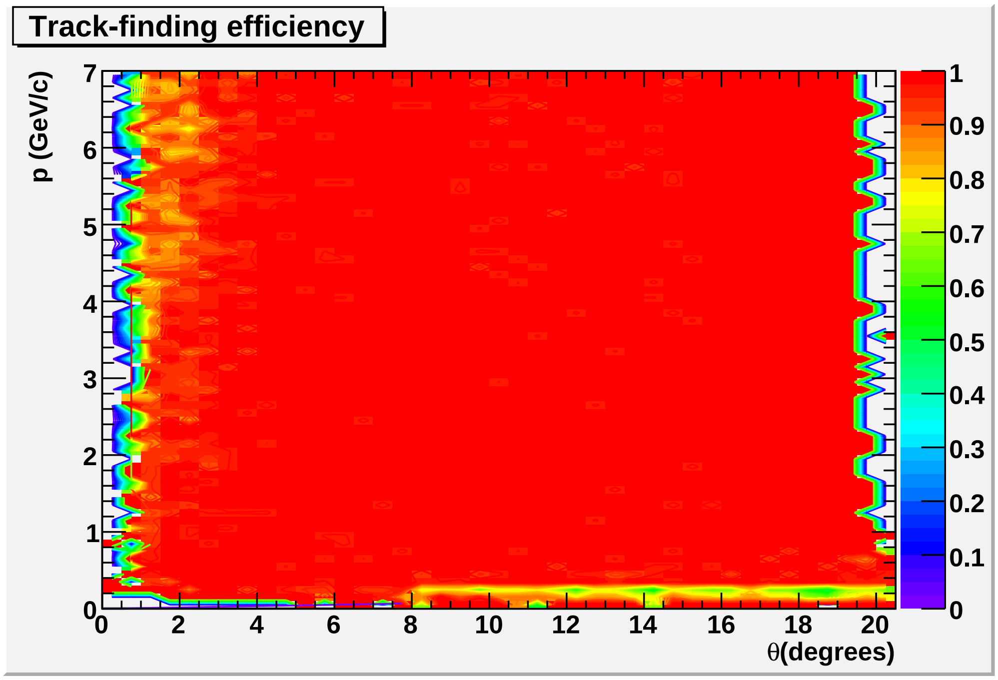

Figure 16: Track-finding efficiency in the FDC for single pion events with no background.

mum number of hits on the thrown track was 5. The overall efficiency integrated over all momenta up to 7 GeV/c and all angles up to ∼ 20° was 97%. We also generated $\gamma p \rightarrow nX(1600), X(1600) \rightarrow \pi^+\pi^+\pi^-$ events using the *genr8* program[2] with a t-slope of 5.0.

---

[2] The *genr8* program is used to generate t-channel events using phase-space via the isobar model. It does not include any background.

3.2.2 Track Finding via Hough Transform

Parallel to the development of the segment-based finder described in Section 3.2.1, a second FDC track finder was developed based on the Hough transform [5]. In this method, the projections of space-points onto the X-Y plane from the FDC are transformed into a space where hits that fall on the same circle will "resonate", giving a peak in the transformed coordinate system. The transverse momentum and ϕ angle are then derived from the location of this peak. See Ref. [9] for more details on an earlier implementation of this algorithm.

The Hough Transform (HT) method is generic in that it only needs a set of 3D space-points as input and does not have any specific dependence on the geometry of the detectors. It does require significantly more CPU time than the seed and segment based methods described in Section 3.1 and the Appendix. Because the HT is generic, it was well-suited for making comparisons between different designs of the FDC. Specifically, to contrast the cathode strip(CWC) design with a wires-only(WW) design. This was done using a simple test case design for the wires-only chamber and the results are presented here.

The wires-only design studied was based on the nominal cathode strip design, but with the cathode strip planes replaced with a ground plane (26 μm aluminized mylar) and the number of chambers doubled. It is important to note that for the solenoidal geometry of the GlueX detector, small stereo angles between wire planes would *not* be preferred due to the ϕ-symmetry and hermiticity requirement. Because of this, the stereo angles were kept large (60°). This large stereo angle increases ambiguities when resolving hits since multiple wire planes must be used to create the space points needed for pattern recognition. Cathode strips are better able to resolve the hit ambiguities locally since all 3 planes view the same avalanche as is shown below. Some of the details of the wires-only and cathode-strip designs are given in Table 1.

Table 1: Wires Only vs. Cathode Strip design parameters

	Wires-Only	Cathode Strips
#of wire planes	48	24
# of cathode strip planes	0	48
wire orientation	0°, +60°,−60°,...	0°, +60°,−60°,...
sense wire spacing	1.116 cm	1.116 cm
wire plane z- spacing	3.0 cm	3.0 cm
Total material(w/ air)	$X/X_o = 1.2\%$	$X/X_o = 3.0\%$

For both the cathode-strip and wires-only designs, a triple plane coincidence was used to define a space point. For the cathode-strips, clusters were found and fit in each of the cathode strip planes. The cathode clusters were then matched with a wire in both position and time to form a triple-plane coincidence. For the wires-only, the space points were constructed by looking at intersection points between adjacent wire planes. Each hit wire was matched with wires in neighboring planes that were immediately upstream and downstream of the hit wire. The space-points that were derived from these intersections were kept only if there existed an intersection point in the opposing, neighboring wire plane that roughly match it in X and Y. With this method, space-points in the wires-only

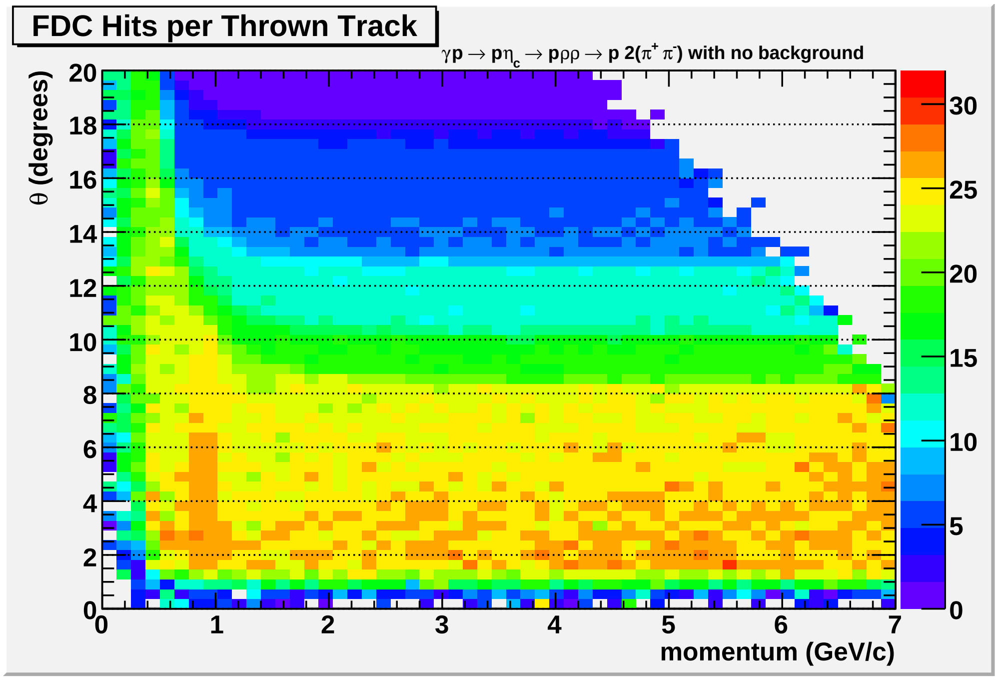

Figure 17: Number of wires hit in the CWC FDC in the absence of background as a function of polar angle (θ) and total momentum.

design were kept only if there was a coincidence in the positions of wires from 3 adjacent wire planes.

The study indicated some clear differences between the designs. The bottom line being that the cathode strip design gives much more powerful constraints on the coincidences between the adjacent planes. With a cathode strip design, all three planes (cathode-wire-cathode) are detecting the same avalanche event. With the wires-only design, each of the wires is observing an independent avalanche and each of these are separated in space. Because of this, the relevant spatial resolution for the cathode strips is on the order of the reconstructed strip resolution (about 200 μm). For the wires-only design, this is on the order of the cell size (about 5 mm). The cathode strips also allow for a tight ($<$ 10 ns) timing cut with each strip and the wire. With the wires-only design, the coincidence time must be on the order of the maximum drift time (about 150 ns).

Figure 17 shows the number of hits per thrown track in the FDC with no background for the cathode-strip design as a function of polar angle and total momentum. The angular ranges where 4,3,2, and 1 package contribute can be seen in the regions below θ=8°, 10°, 13°, and 18° respectively. Realistically, a minimum of 5 hits is needed to reconstruct a track in the FDC using using the cathode-strip design.

Figure 18 shows a single event in both the cathode strip and wires-only designs with and without the found tracks drawn. These illustrate the condition where the ghost hits confuse the Hough algorithm for the wires-only design resulting in lots of ghost tracks. The cathode strips design is more immune from this condition.

Figure 19 shows an example of how the ghost hits arise from unresolved ambiguities in the FDC wires-only design. The real hits are drawn with black circles. The red

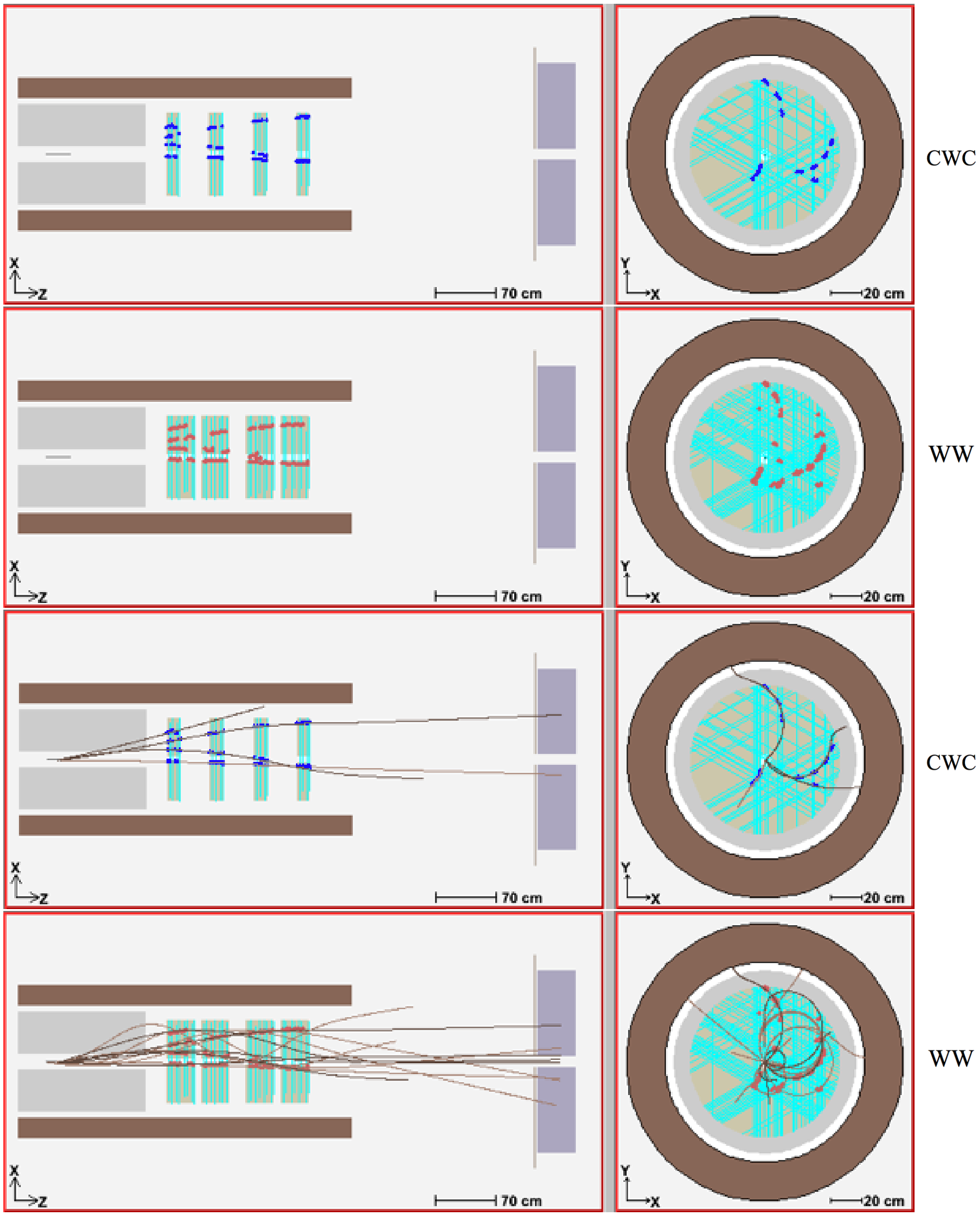

Figure 18: Plots showing a single event for both the cathodes strip design and the wires-only design. The top 2 drawings show the space-points without the tracks drawn and the bottom 2 with the tracks. The 1st and 3rd plots (with the blue hits) represent the cathode strip design while the 2nd and fourth (with the orange hits) represent the wires-only design. This shows how the extra hits in the wires-only design arising from unresolved ambiguities confuse the track finder, causing it to find lots of ghost tracks.

squares indicate coincidences between the cathode strips and wire plane. The triangles represent intersection points between adjacent wire planes with red triangles representing intersection points between the middle plane and its upstream neighbor and the blue with its downstream neighbor. For the event shown, there were 4 tracks in the chambers. One can see that three of these tracks hit 3 different wires that happen to intersect one another and one location in the X-Y plane. These intersections are labeled "Ghost Hits".

Figure 20 compares the number of track candidates found in the nominal dual cathodes design and a wires only design for 5 track events. There were an average of 3.1 tracks per event in the FDC for the data set used. The plots indicate that many more ghost candidates were found using the wires only design than the cathode strips design. It should be noted that this does not necessarily indicate a limitation of the wires only design that could not be overcome with more effort. However, since the exact same Hough Transform algorithm was used and the exact same set of generated events, it suggests the algorithm needed to implement *this* wires only design would likely be more complex than that needed for the cathode strips design.

Because of this, the wires-only design was much more prone to "ghost" hits than the cathode strip design. This led to significantly more ghost tracks in high multiplicity events. One can also see an indication of the quality of the space points in Figure 21, where the momentum resolution of the *candidates* (not the final fit tracks) is shown for the wires-only and cathode strip designs using the exact same Hough Transform algorithm. For wires-only design, the effective position resolution of the intersection points is worse as can be seen in the larger dependence on momentum. The points labeled "Cathodes Seed" show no dependence on momentum indicating the position resolution for those points is very good. This is indeed the case since those points came from the segment-based finder which corrected for the Lorentz effect and used the drift time in the fit. Since no additional smearing was applied to the hits used to make this plot, the "Cathodes Seed" points had perfect position resolution once all of the effects were corrected for (see the Appendix). Finally, the "Cathodes Hough" points in figure 21 indicate some effective position resolution, but less than that seen in the "Wires Only Hough". This is because these points do not correct for the Lorentz deflections and so have a resolution along the wire on the order of 1mm. Like the "Cathodes Hough" points though, they have a position resolution perpendicular to the wire that is on the order of the (half) cell size or about 5mm. Therefore, the overall position resolution of the "Cathodes Hough" hits is better than that of the "Wires Only Hough" hits. Note that while these effective position resolutions are responsible for the quality of the track parameters obtained from the fitter, they are not necessarily the resolutions used to form coincidences between adjacent planes as indicated above.

Figure 22 shows the single track finding efficiency for 5 track events as a function of momentum in the presence of various levels of EM background for forward going tracks ($1^\circ \leq \theta \leq 12^\circ$). This indicates that the efficiency tends to drop as the background increases. Figure 23 shows a zoomed in view of the points at p=3 GeV/c for both the cathode strip and wires-only designs. This plot indicates a single track efficiency of about 91% for the wires-only design at high luminosity running (10^8 tagged γ/s).

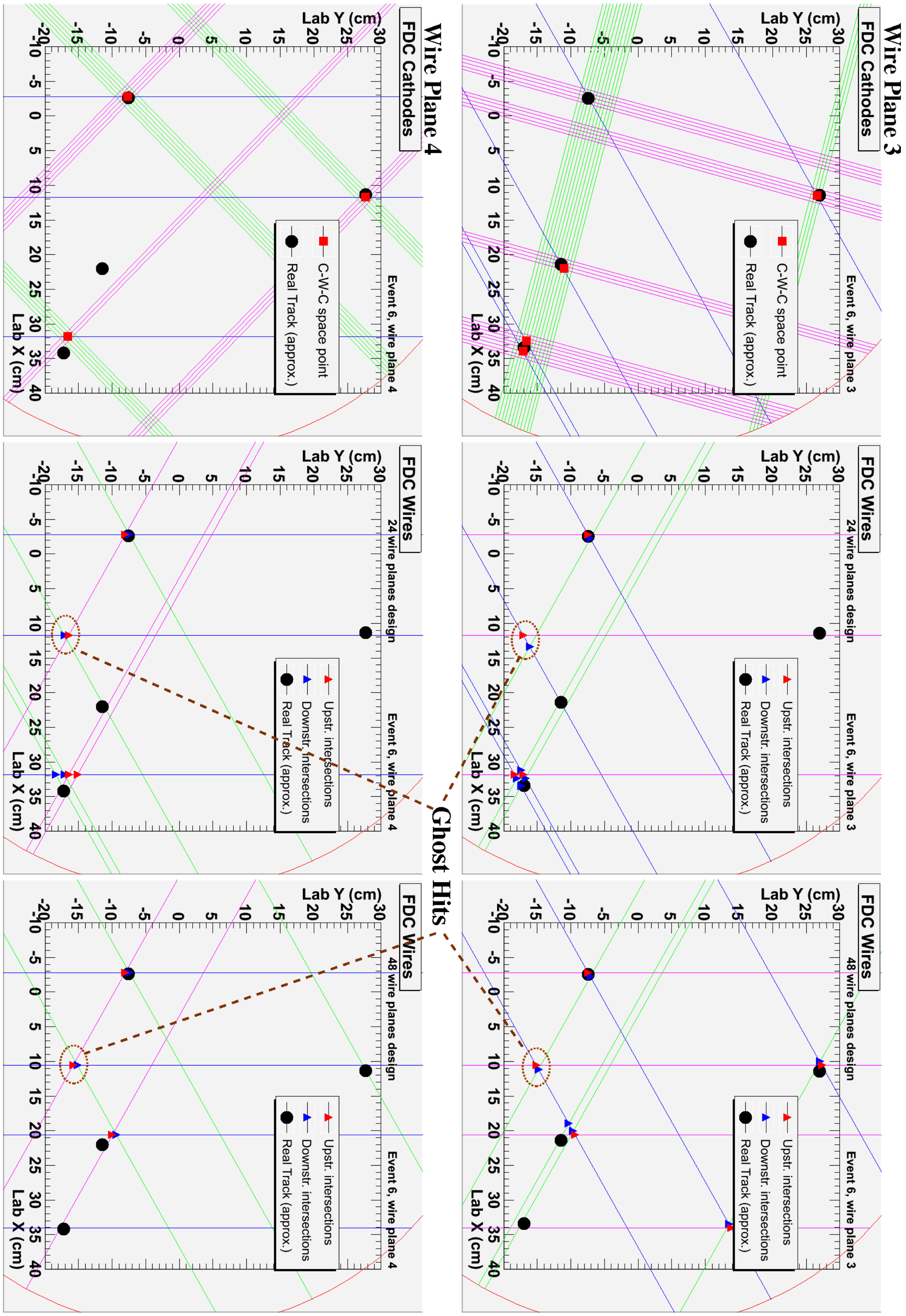

Figure 19: These pictures illustrate the problem of ambiguous hits in a wires-only design relative to a cathode strip design. Please see the text for more details.

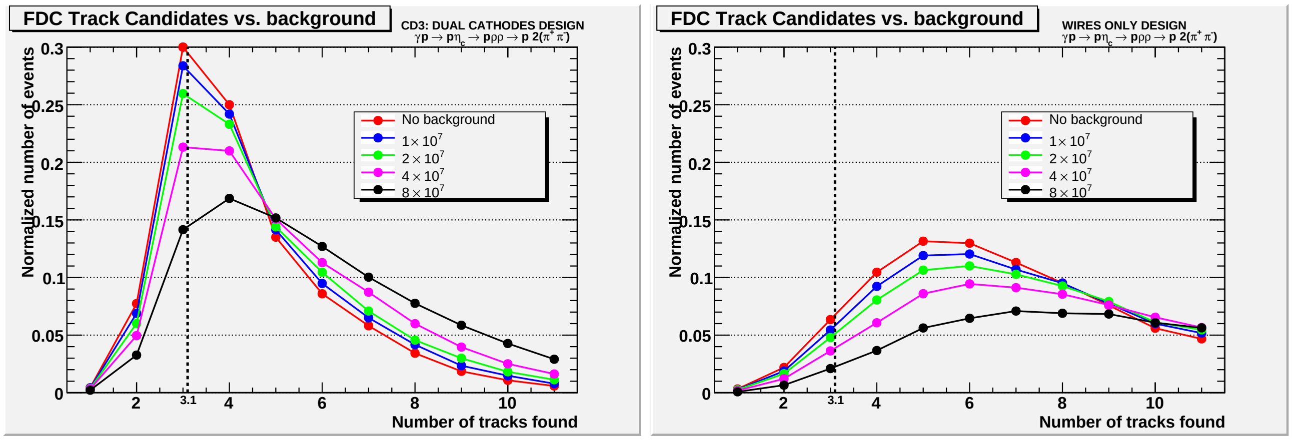

Figure 20: Total number of track candidates in the FDC for 5 track events. The plot on the left side was made from simulated data using the nominal, dual cathodes design, while the plot on the right used a wires-only design. The average number of tracks in the FDC per event was 3.1 as indicated by the dotted black lines.

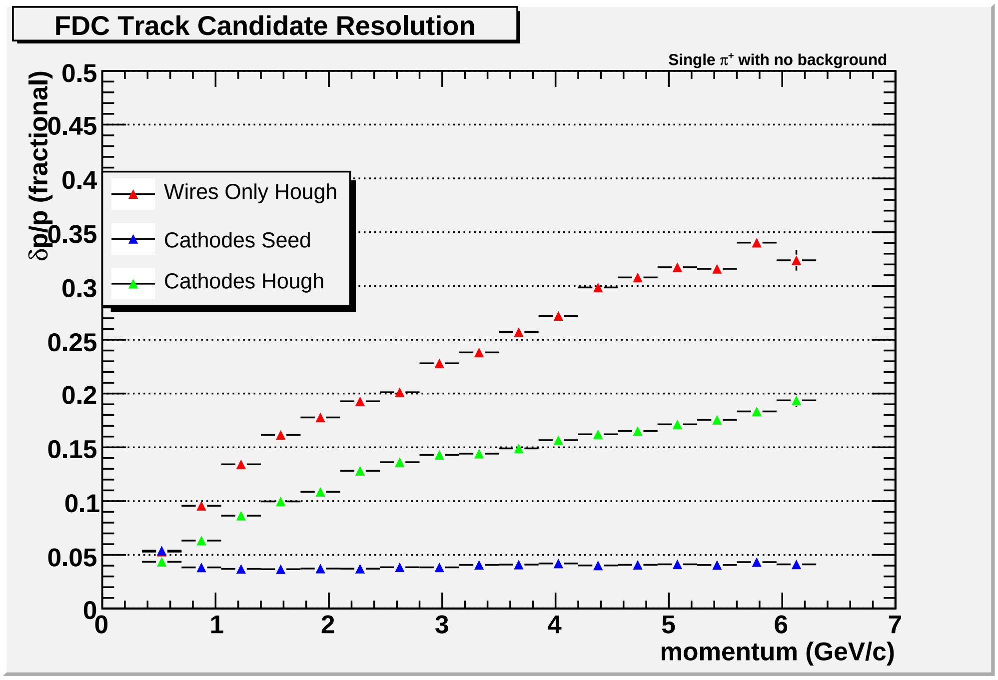

Figure 21: Resolution of forward-going track candidates in the FDC for the 2 different track finding methods and two detector geometries (*Cathodes Seed* only applied to CWC geometry). These indicate the quality of the parameters going into the track fitter. Note that there was no additional smearing of the drift times for this data. The *Cathodes Seed* points came from the segment-based finder, which corrected for the Lorentz effect and did a more sophisticated fitting of the points.

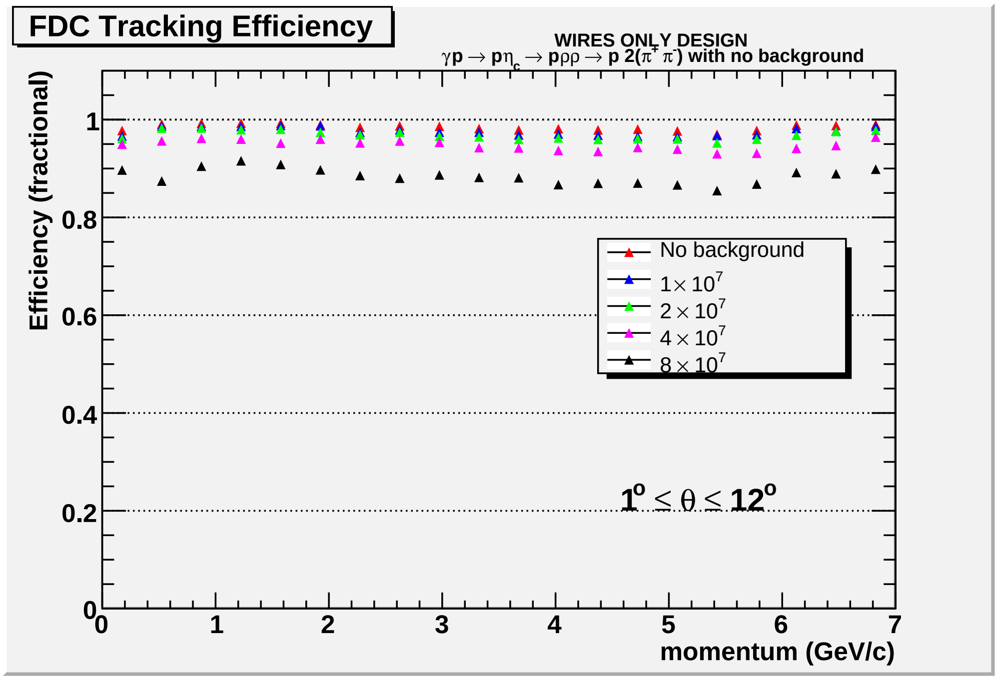

Figure 22: Track finding efficiency in the FDC wires-only design as a function of momentum in the presence of various levels of EM background. The labels indicated in the legend represent the number of tagged γ/s.

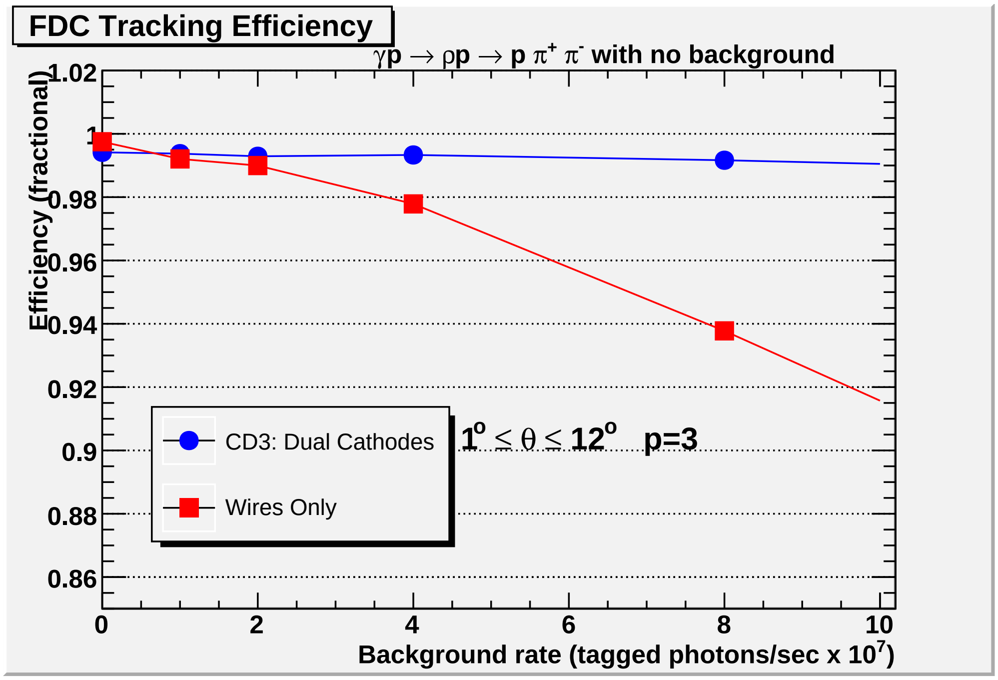

Figure 23: Track finding efficiency for 3 GeV/c tracks comparing the wires-only design with the cathode strip design as a function of the EM background. The drop in efficiency for the wires-only design is due to the ghost tracks “stealing” hits from real tracks such that they are not found.

4 Tracking Resolutions

4.1 Resolutions From Monte Carlo

4.1.1 The Track Fitter

The track fitter used for the current study was modified somewhat from that used in the previous study described in Ref. [6]. The current fitter still uses the Newton-Raphson matrix inversion method to do a global fit [7]. The three most significant changes made to the fitter for the current study are:

1. A round of hit-based track fitting is done prior to the time-based fits (a'la CLAS)
2. A left/right ambiguity choice was implemented in a similar manner to the tracking algorithm used by CLAS in Hall-B
3. Cathode planes from the FDC were not used.

The target constraint comes in as the distance of closest approach (DOCA) that the track makes with a 3 cm segment of the beam line if the trajectory is extended both forward and backward in time. The 3 cm segment is centered on the z-vertex value returned in the track candidate. The constraint is fuzzy in that it is implemented as an additional term in the χ^2 using a sigma of 1 mm as the uncertainty of this DOCA. As a reminder, the beam spot size at the target will have a diameter of approximately 1.75 mm. The DOCA point, however, will be on average closer to the beam line than the interaction point. This method ignores for now situations of detached vertices originating from in-flight decays or long-lived baryon decays (e.g. Lambdas).

The fitter was adapted to more closely follow the CLAS model for track fitting as recommended by the March 2007 review committee (Ref. [8]). In the current fitter, each track undergoes up to 3 iterations of hit-based fitting first, where only the wire locations are used and the drift times are ignored. After this, the resulting track is used to make a choice as to which side of the wire the track passed. This information is then used to collapse what could be considered a fuzzy ring around the wire into a fuzzy line on one side of the wire. The fuzziness comes from the known position resolutions: 150 μm for the CDC and 200 μm for the FDC.

For the current fitter, the cathode plane information was not used as it had been previously. This was primarily because the data now (properly) includes Lorentz deflections along the wire due to the magnetic field as described in Section 3.2. While these deflections can be corrected for by using the knowledge of which side of the wire the track passed, the software had not yet been developed and tested to the point where it could be included in this document. Including the strip information in the fitter should improve the resolution by as much as a factor of $\sqrt{2}$ in the very forward region. This would be the case if the 2 combined cathode planes provide a measurement of the tracks position along the direction of the wire that is comparable in resolution to that of the drift time.

The fit is done using multiple passes (up to 10 for time-based fitting) with an option to redo a fit with a track of opposite charge should the original candidate not converge properly or if the track has a χ^2 greater than 2.0.

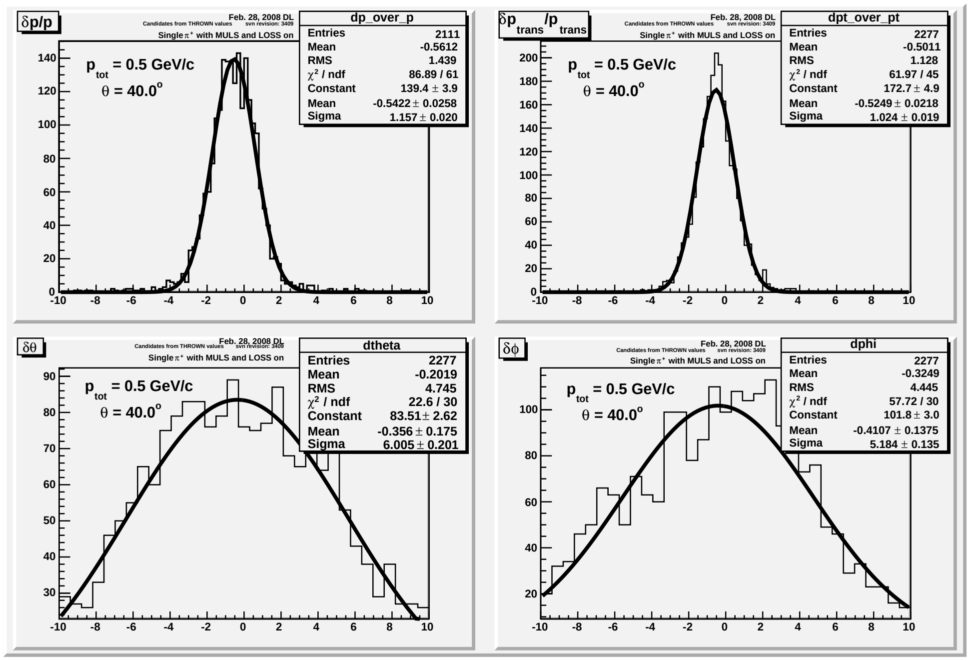

Figure 24: Fit results for a single bin at $p_{tot} = 0.5GeV/c$ and $\theta = 40°$. The fits are all done with a single Gaussian and the widths are what is plotted in Figures 28-40.

4.1.2 Single π^+ Track Resolutions

This section documents the tracking resolutions for single π^+ tracks. For this study, approximately 55 million events were generated. Each had a single π^+ and no background was included. The π^+'s were thrown isotropically with momentum ranging from 0 to 7 GeV/c and in the angular range $0° \leq \theta \leq 160°$. Tracks were distributed evenly in azimuthal angle ϕ.

For the purposes of this study, the track candidates were taken from the thrown values. The simulated data were separated into bins in both total momentum and polar angle. For figures 24-27 a bin size of $152MeV/c$ by $1\frac{1}{3}^{\circ}$ was used while for figures 28-42 used a bin size of $70MeV/c$ by $\frac{2}{3}^{\circ}$. For each bin, the resolutions of the total momentum, transverse momentum, polar angle, and azimuthal angle were obtained by fitting a single Gaussian to the respective distributions. Figures 24-26 show the fits for 3 of the bins as examples. The single Gaussian functions used for the fits seemed to do a reasonable job of describing the distributions.

Figure 27 shows the pulls of the $\delta p_t/p_t$, $\delta\theta$, and $\delta\phi$ distributions for a different data set than what was used to derive the initial set of variances described above. These should be Gaussian in shape with $mean = 0$ and $\sigma = 1.0$. The fact that they are simply means the mechanisms for creating and reading the tables are working. Also shown in the lower right of Figure 27 is a χ^2 distribution generated using the 3 pulls on an event by event basis. In other words, for each event, the $\delta p_t/p_t$, $\delta\theta$, and $\delta\phi$ pulls were added to form a χ^2 and then divided by the number of degrees of freedom which in this case was 3. A cut

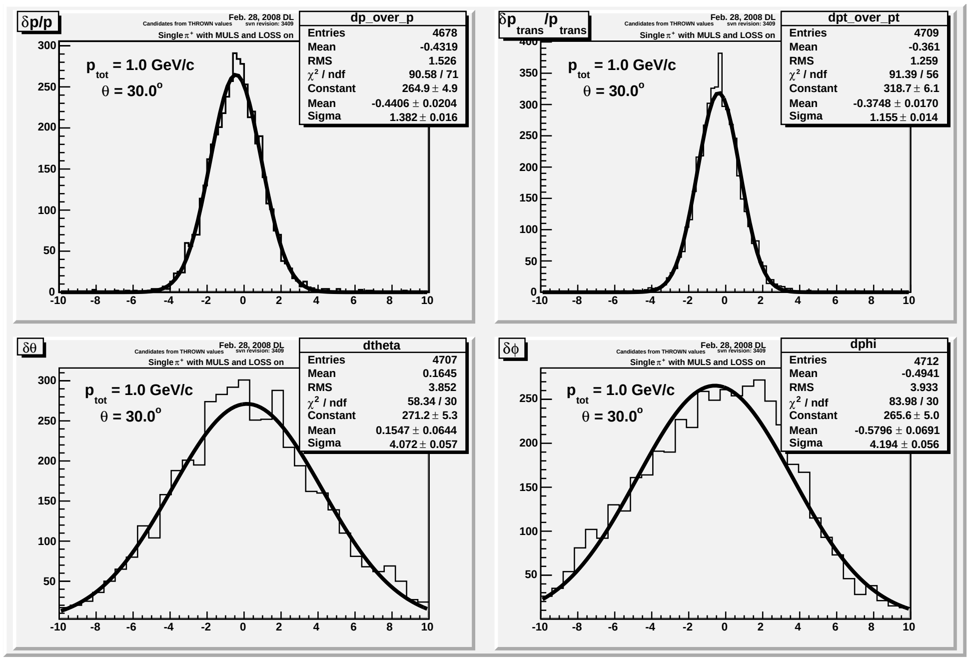

Figure 25: Fit results for a single bin at $p_{tot} = 1.0 GeV/c$ and $\theta = 30°$. The fits are all done with a single Gaussian and the widths are what is plotted in Figures 28-40.

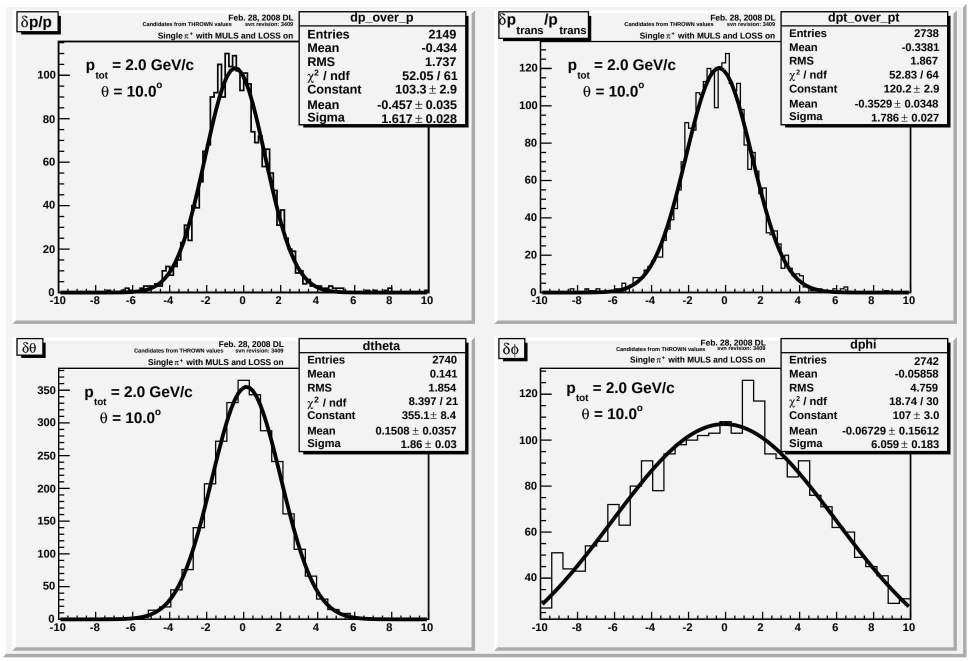

Figure 26: Fit results for a single bin at $p_{tot} = 2.0 GeV/c$ and $\theta = 10°$. The fits are all done with a single Gaussian and the widths are what is plotted in Figures 28-40.

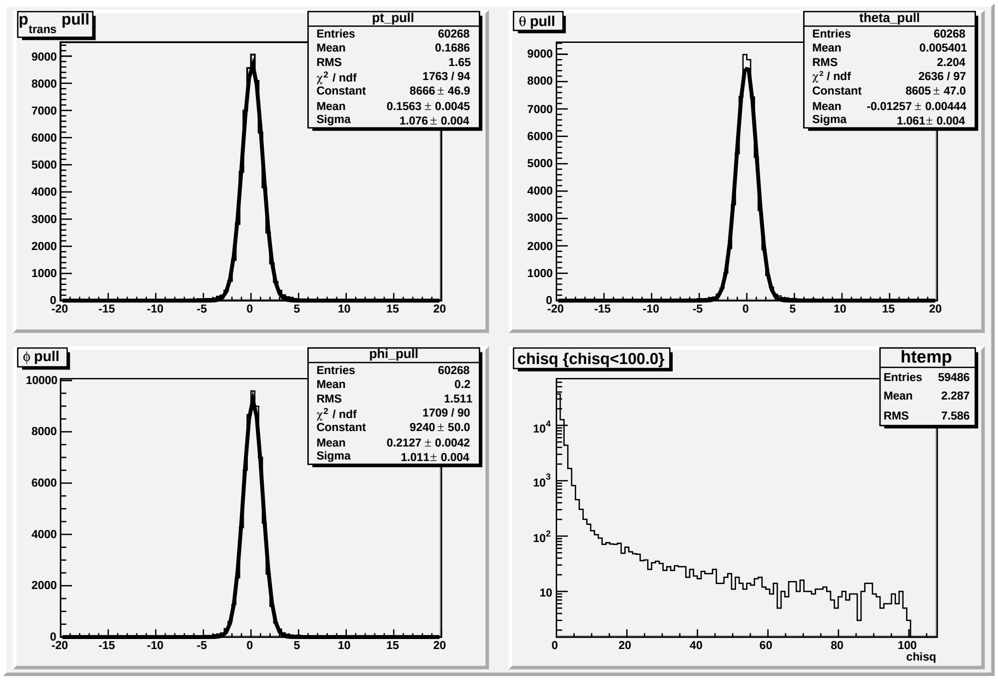

Figure 27: Pull distributions for p_t, $\delta\theta$, and $\delta\phi$. The χ^2 distribution is made by adding the 3 pulls and dividing by the number of degrees of freedom (in this case 3) for each event.

on this χ^2 value will eventually be used to determine the overall tracking efficiency for Monte Carlo data.

Figures 28-31 show both the total and transverse momentum resolutions as a function of p_{tot} and θ. Figures 28 and 29 contain essentially the same information as Figures 30 and 31, only plotted in a slightly different way and with an inset zoomed in on the forward angular region.

Figure 32 shows the transverse momentum resolution as a function of polar angle for particles of various momenta. The multi-peaked structure arises from the simultaneous loss of hits (and path length) in the CDC and gain of hits in the FDC as one scans down in angle. Dotted vertical lines are drawn on the plot that indicate locations of each of the FDC packages and the CDC endplate to aid understanding of the features. Specifically, the resolution gets worse with lower angles below 29° when particles begin to exit the CDC through the endplate. Particles leaving through the endplate will not reach the outer layers of the CDC and so will have fewer hits. Also, the path length of of these tracks through the CDC will be smaller for smaller angles which also works to degrade the resolution. At 22°, tracks begin to hit the first FDC package and the resolution quickly gets better again. Tracks at about 17° pass through all of the layers of the first FDC package, but do not pass through any other FDC package until they get down to 15.5°. In this region between 17° and 15.5°, path length and hits continue to be lost from the CDC causing the resolution to worsen with smaller angles. This pattern repeats as each of the FDC packages comes into play causing the multi-peak structure. Note that this particular structure was not seen in the resolutions obtained for last year's geometry (see figure 12

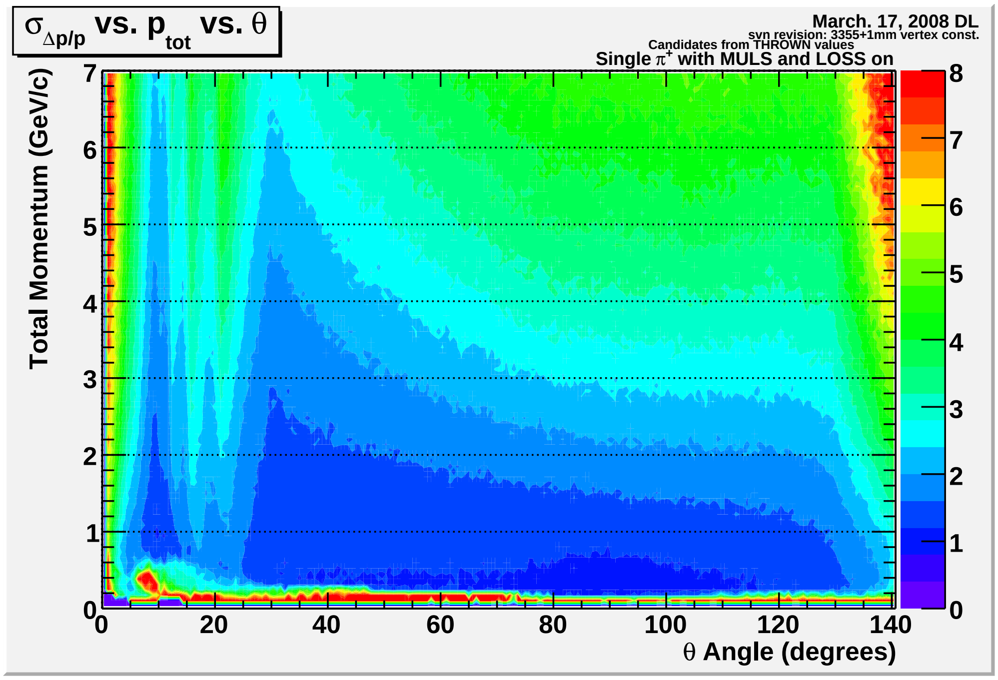

Figure 28: Total momentum resolution map as a function of total momentum and polar angle at the vertex. The z-axis is in percent.

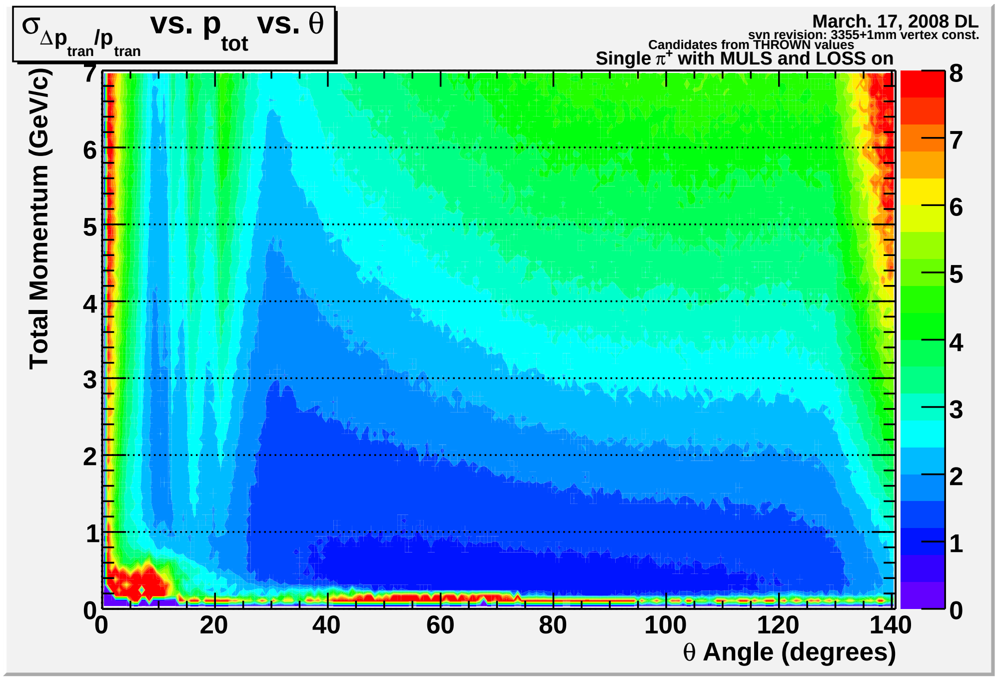

Figure 29: Transverse momentum resolution map as a function of total momentum and polar angle at the vertex. The z-axis is in percent.

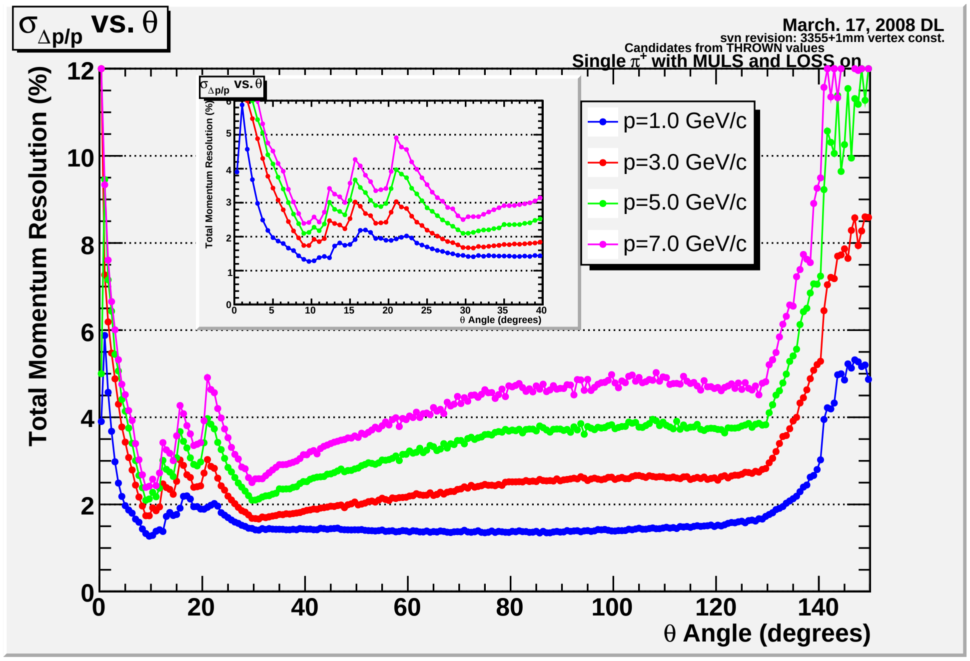

Figure 30: Total momentum resolution as a function of θ for various values of the total mometum. These are just projections of the 2D histogram in Figure 28.

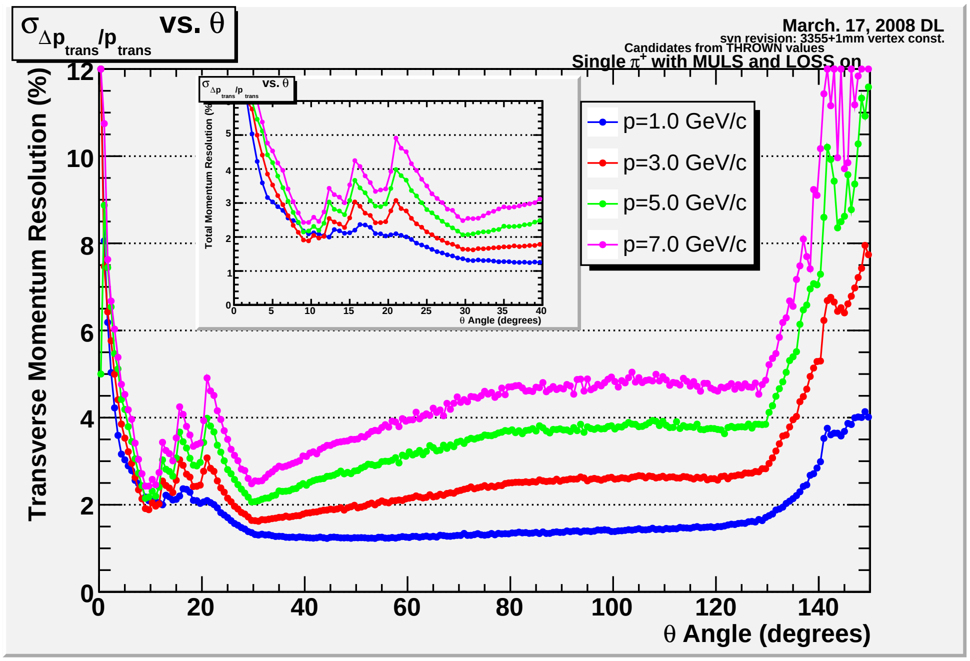

Figure 31: Transverse momentum resolution as a function of θ for various values of the total mometum. These are just projections of the 2D histogram in Figure 29.

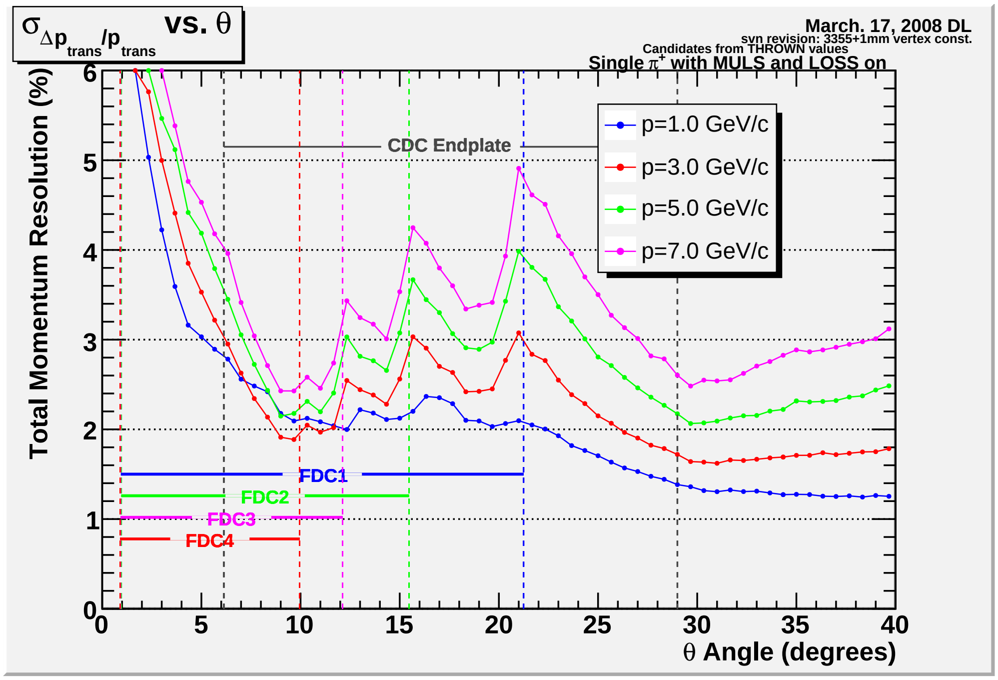

Figure 32: Transverse momentum resolution as a function of polar angle in the forward region.

and Ref. [6]). This was because the FDC package positions were further downstream and so covered a smaller range of angles. Also, the simulated data set was much smaller for last year's geometry and so had much wider bins which averaged out any such structure that might have otherwise been seen.

Figures 33-40 show both the polar (θ) and azimuthal (ϕ) angular resolutions as a function of p_{tot} and θ. Figures 33 and 34 contain essentially the same information as Figures 37 and 40 only plotted in a slightly different way.

5 Summary

Studies have been done with the latest designs of the CDC and FDC chambers. The overall track finding efficiency is good in both the CDC and FDC, as well as in the transition region between the two. Studies were done where a realistic EM background was mixed in with single π^+ tracks and various levels corresponding up to 8×10^7 tagged γ/sec with no significant loss in the track finding efficiency (i.e. $> 98\%$).

A study was done to contrast the cathode-strip design with a wires-only design for the FDC. The cathode-strip design had 3.0% of a radiation length of material in the active area while the wires-only design had 1.2%. The wires-only design is a practical minimum on the amount of material needed for a detector.The study indicated that the wires-only design was more susceptible to ghost tracks than the cathode strip design. This was due to the cathode strips allowing for much tighter coincidence cuts in both position and timing of individual track hits.

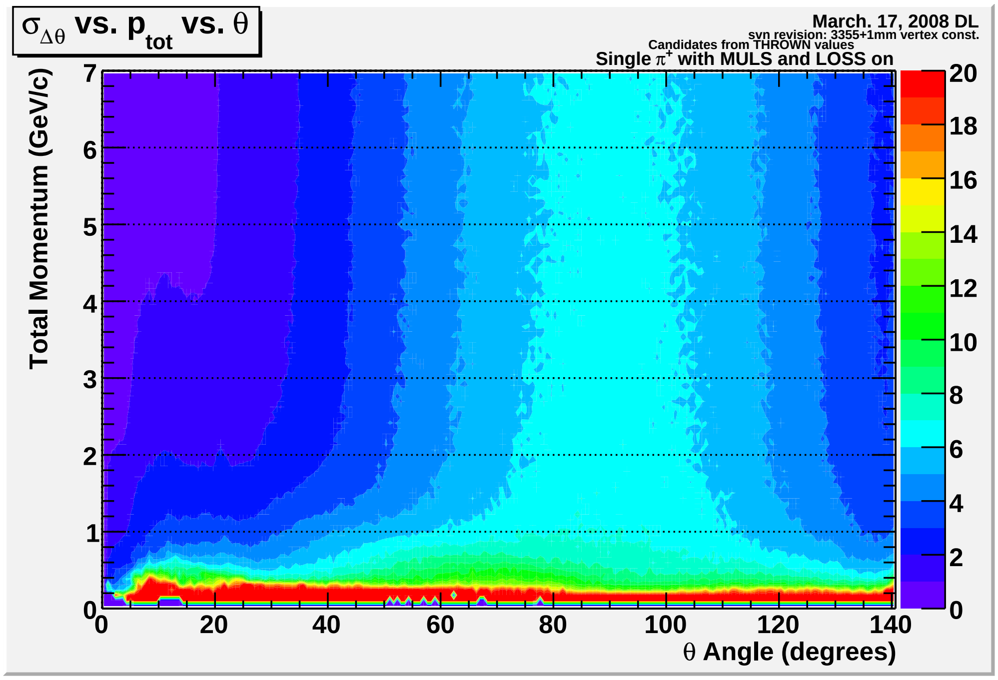

Figure 33: Polar angular resolution map as a function of total momentum and polar angle.

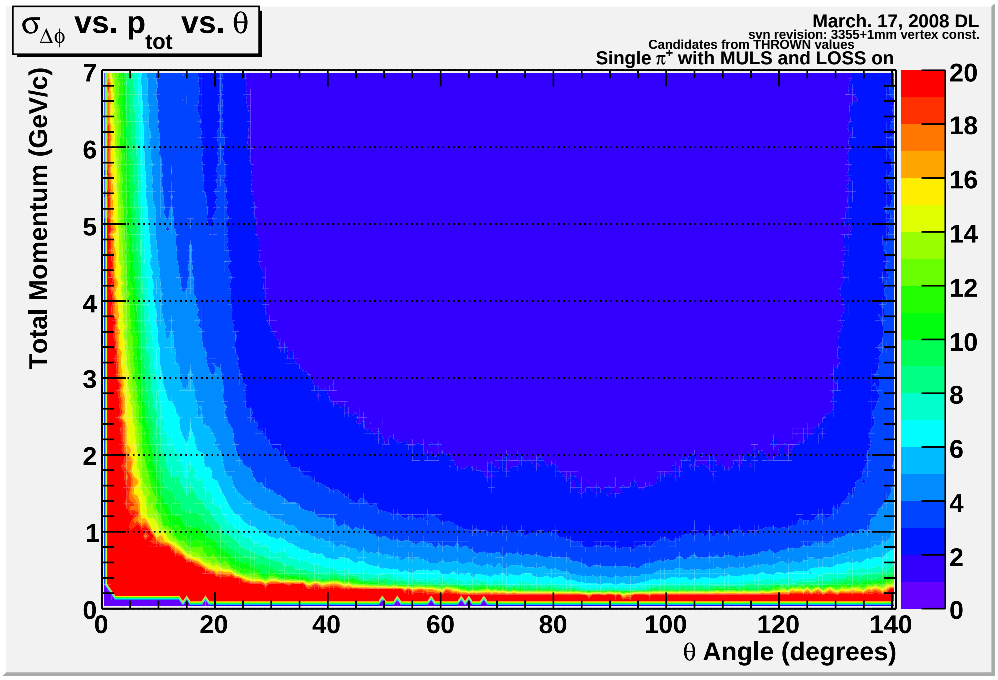

Figure 34: Azimuthal angular resolution map as a function of total momentum and polar angle.

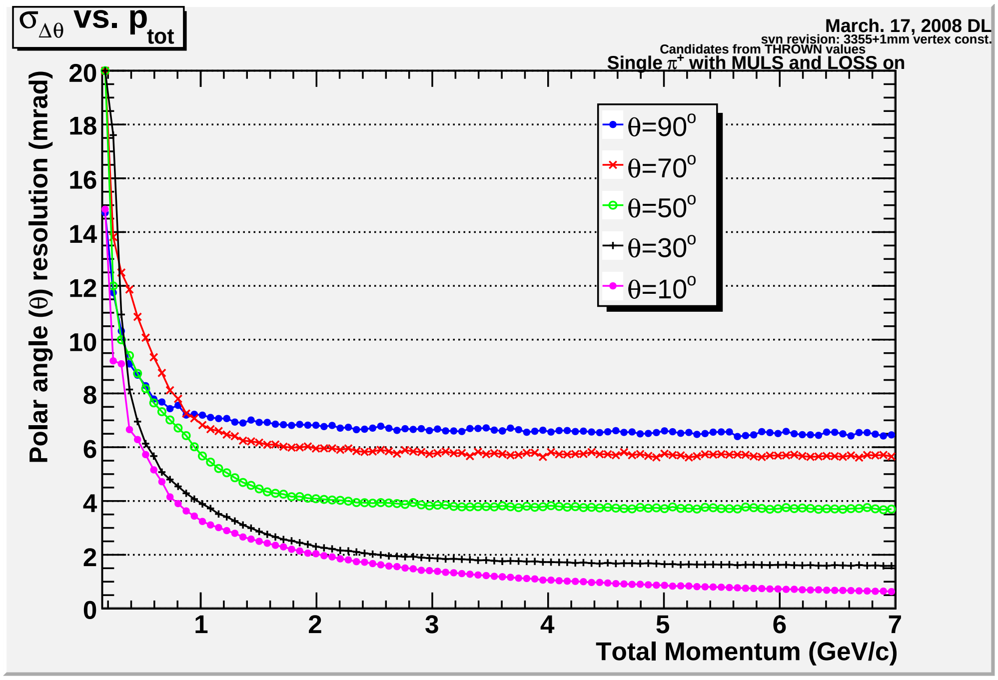

Figure 35: Polar angular resolution as a function of total momentum. These are projections from Figure 33.

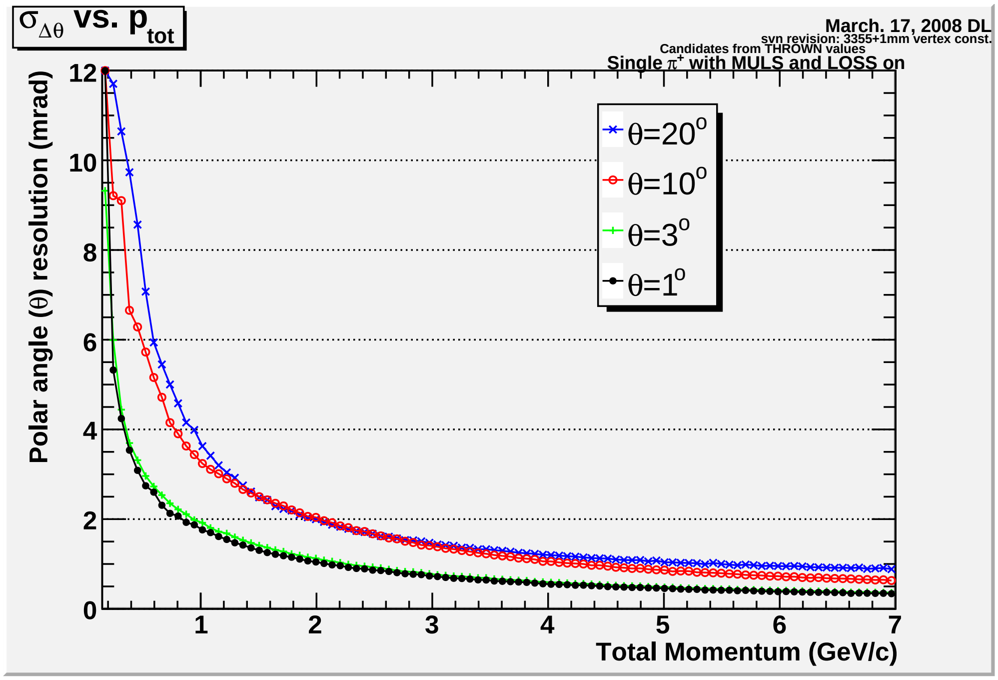

Figure 36: Polar angular resolution as a function of total momentum in the forward region.

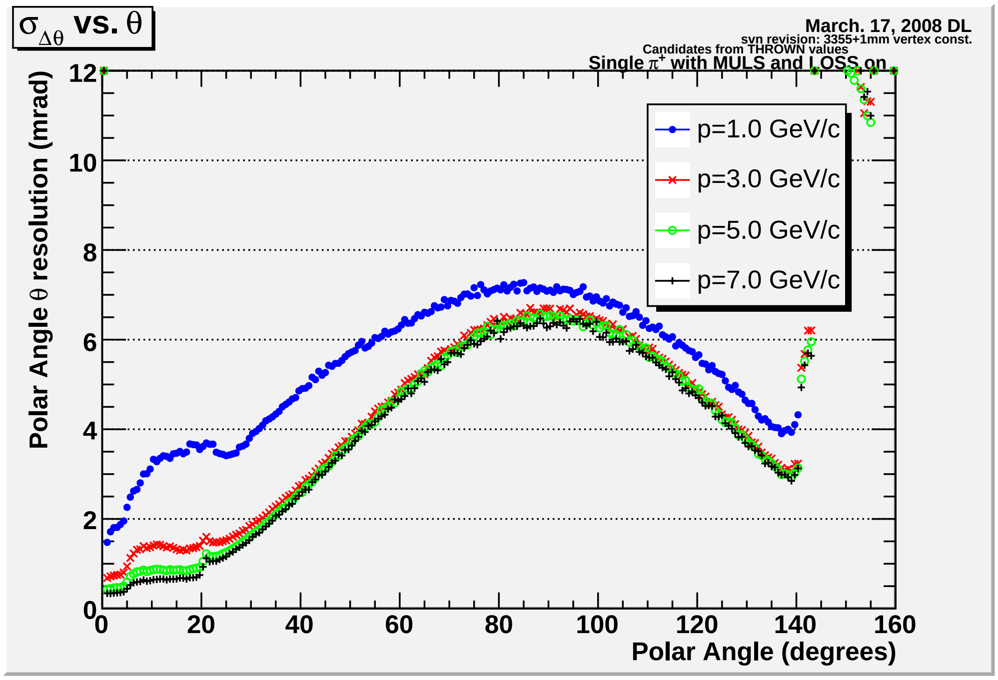

Figure 37: Polar angular resolution a function of polar angle θ. These are projects from Figure 33.

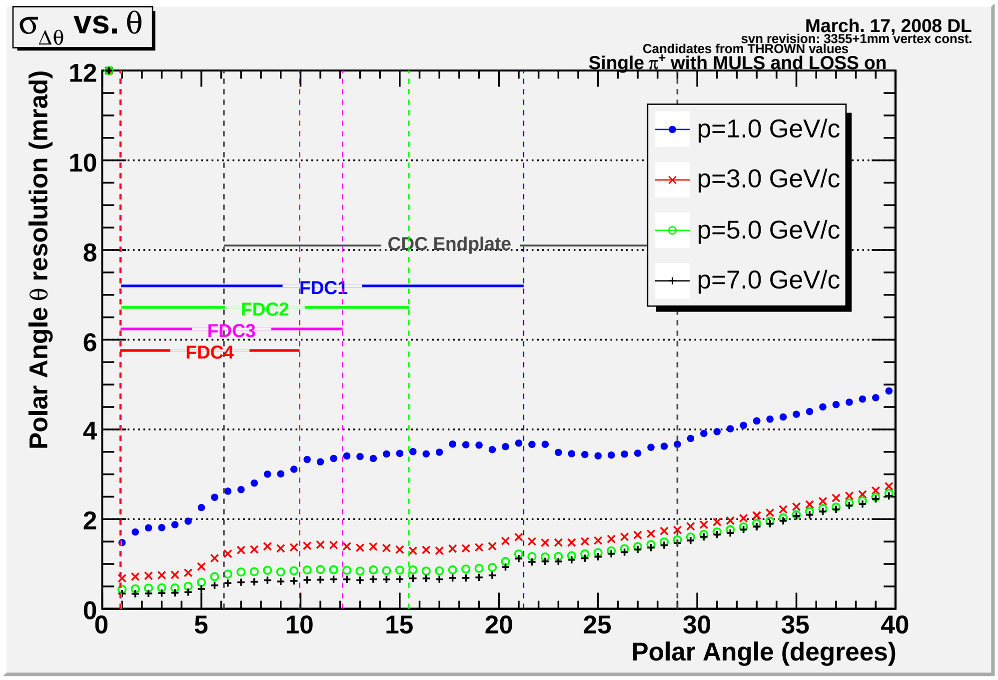

Figure 38: Polar angle resolution as a function of polar angle in the forward angle.

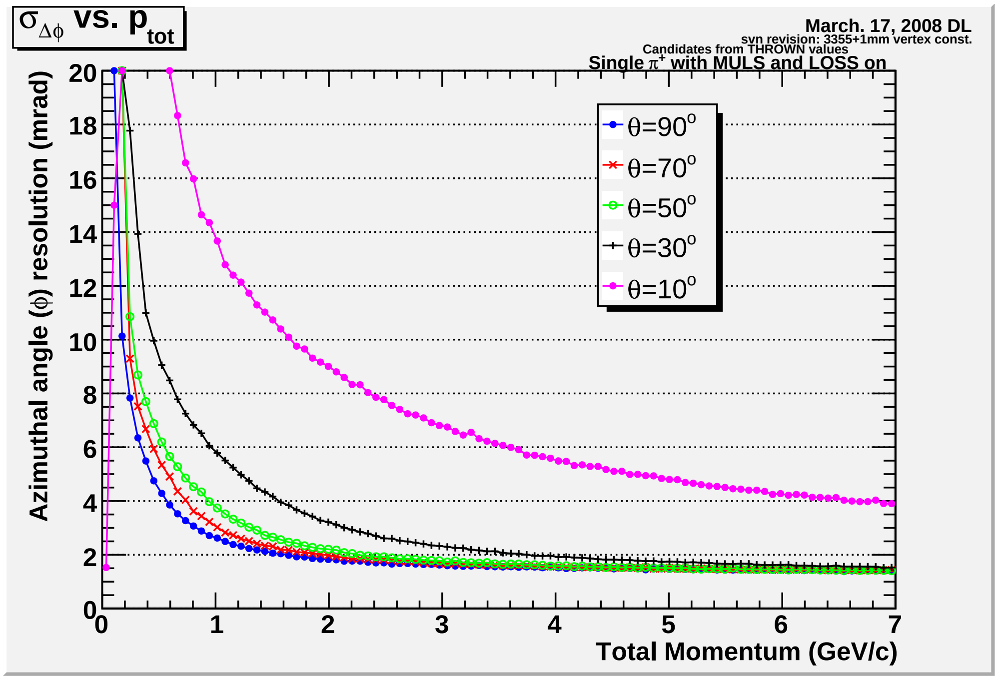

Figure 39: Azimuthal angular resolution a function of total momentum. These are projections from Figure 34.

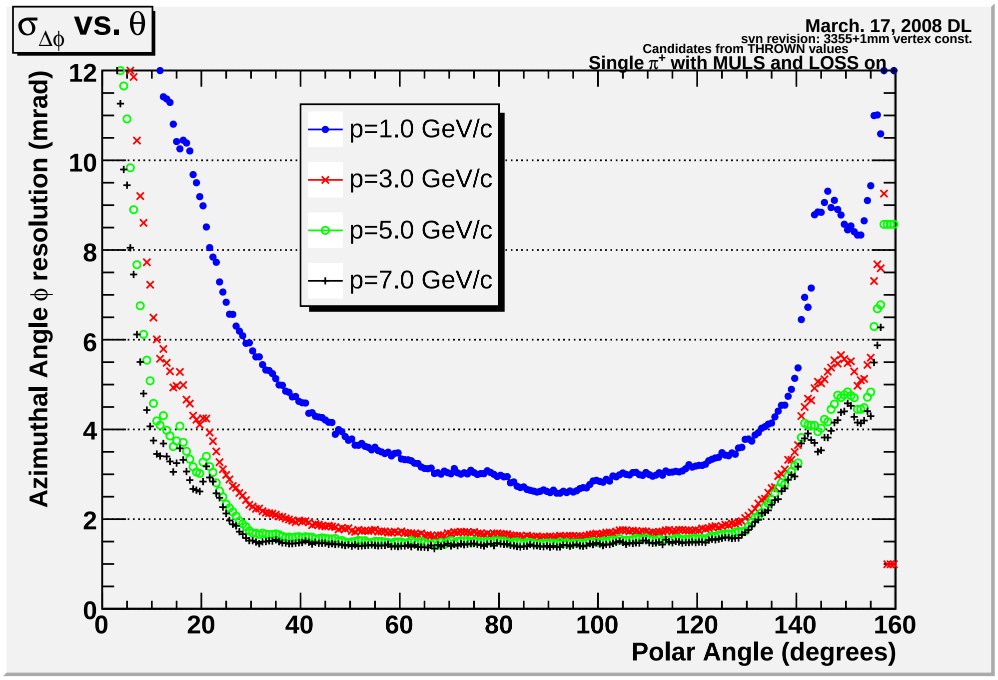

Figure 40: Azimuthal angular resolution as a function of polar angle θ. These are projections from figure 34.

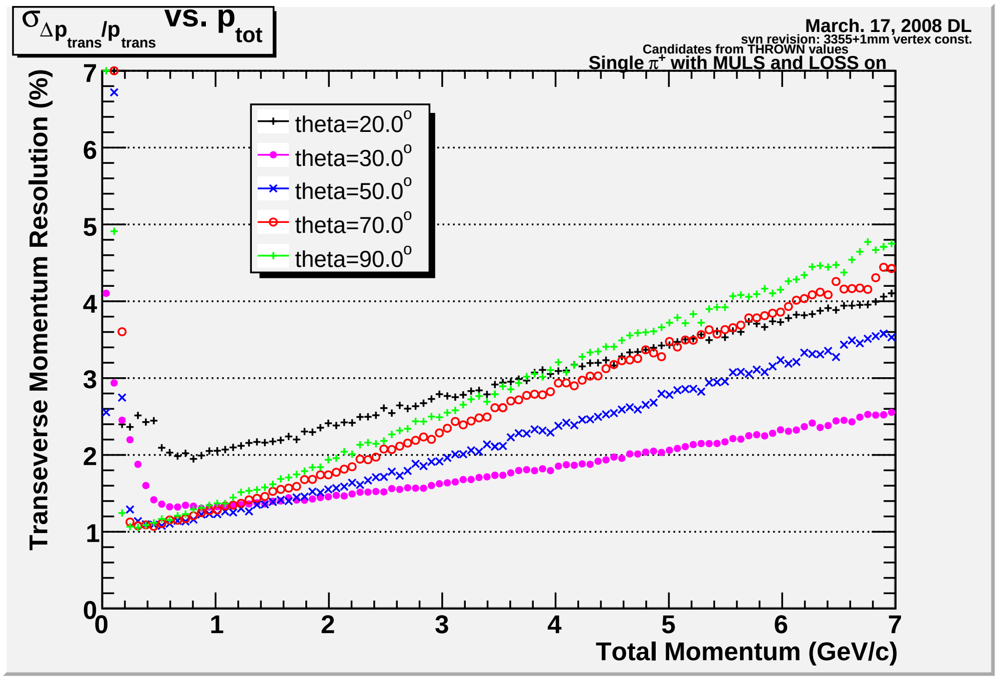

Figure 41: Transverse momentum resolution as a function of total momentum.

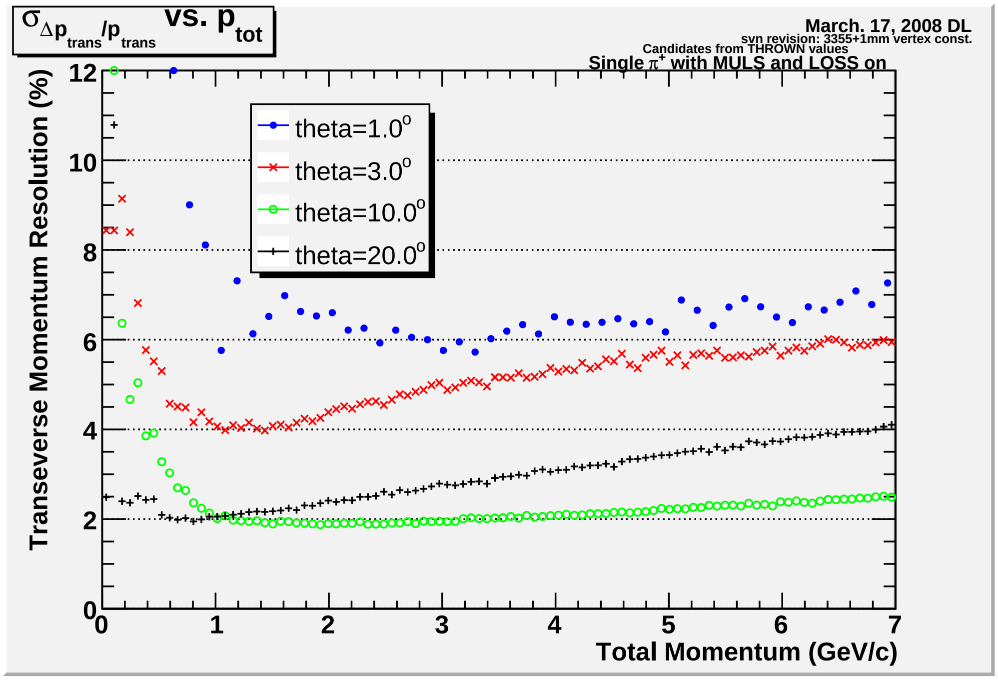

Figure 42: Transverse momentum resolution as a function of total momentum in the forward region.

Tracking resolutions for single π^+ events were derived using the full GEANT-based Monte Carlo. Resolutions were shown for the transverse momentum, as well as the polar and azimuthal angular resolutions. The transverse momentum resolution $\delta p_T/p_T$ is 2-4% for tracks with less than 5GrV/c momentum at $5^\circ < \theta < 130^\circ$. The polar angular resolution is 1-7 mrad for pions with momentum >1 GeV/c. The azimuthal angular resolution was better than 2 mrad for pions with momentum >2 GeV/c.

6 Still To Do

Work that is still need on the simulation and reconstruction for charged particle tracking:

- Optimization of FDC package positions and CDC length
- Incorporate multiple scattering errors correctly in fitter (e.g. Kalman Filter)
- Implement energy loss in swimmer for low momentum tracks
- Study full impact of vertex constraint on resolutions
- Tabulate resolutions for other particles (protons, kaons, electrons)
- Improve ghost hit and ghost track rejection in finders

References

[1] D. Lawrence, S. Taylor *GlueX Simulation Geometry Version 4.0* GlueX-doc-853 (2007)

[2] M. Shepherd *GlueX Calorimetry Simulation* (talk) GlueX-doc-984-v3 (2008)

[3] R. Frühwirth, A. Strandlie, and W. Waltenberger, *Helix Fitting by an Extended Riemann Fit*, Nucl. Intr. and Meth. A**490**(2002) 366-378.

[4] R. Veenhof, *The GARFIELD Program: Simulation of Gaseous Detectors*, http://garfield.web.cern.ch/garfield/ (1984).

[5] R. Frühwirth, M. Regler, R.K. Bock, H. Grote, D. Notz *Data Analysis Techniques for High-Energy Physics 2nd Ed.* Cambridge Monographs on Particle Physics, Nuclear Physics and Cosmology 11 (2000) chapter 2

[6] D. Lawrence *Track Fitting in GlueX Development Report III* GlueX-doc-761 (2005)

[7] R. Mankel *Pattern Recognition and Event Reconstruction in Particle Physics Experiments* Rep. Prog. Phys. **67**(2004) 553-622

[8] D. Christian, M.Kelsey, D. Hasell, and B. Mecking, "Hall B and Hall D Drift Chamber Review Report", March 16, 2007.

[9] D. Lawrence *Track Finding in GlueX Development Report II* GlueX-doc-528 (2005)

APPENDIX : Segment-based track Finding and Fitting

Preliminary track parameters are determined in the segment-based FDC track finder by fitting the hits in each package using a helical track model. The method employed is the Riemann Helical Fit [3]. The fit is divided into two basic components, a circle fit and a line fit. In a uniform magnetic field pointing along the beam-axis, hits on a track form a circle when projected onto a plane normal to the beam-axis. The circle fit maps points on this circle to points on a Riemann surface, specifically a circular paraboloid, as illustrated in Figure 43. The problem of finding the center and radius of the circle is transformed to the problem of finding the normal of the plane, defined by the projected points, slicing the Riemann surface. We include a “fuzzy” fake point at the center of the target with a variance of 0.1 cm^2 transverse to the beam. The fit is extended to a helical path by recognizing that the arc length between successive measurements around the circle maps directly to a change in position along z. Linear regression of the arc length s as a function of z determines the tangent of the dip angle λ.

The determination of the full track candidate parameters is performed in three steps. The first step is to compute a reference track segment using hit-based information (no

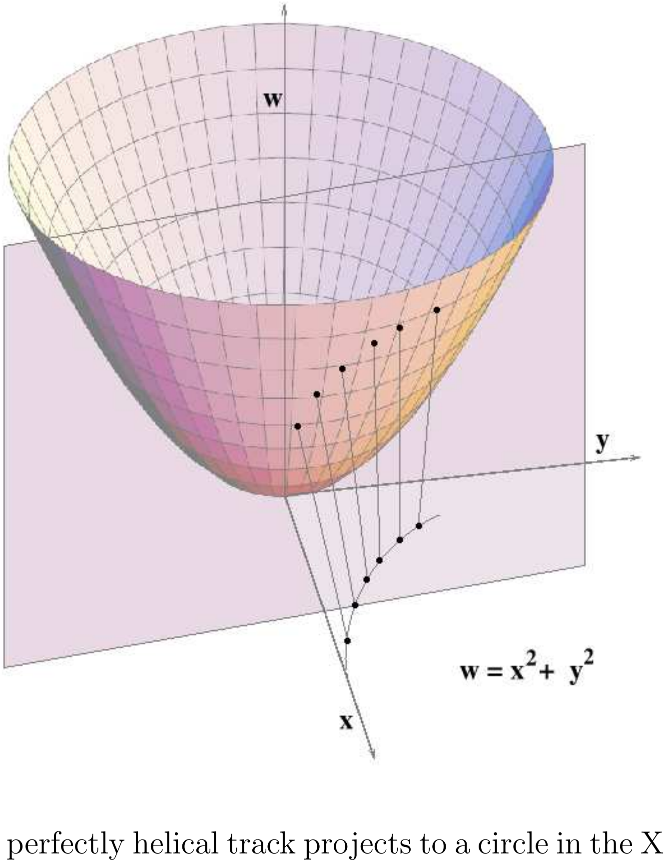

Figure 43: A perfectly helical track projects to a circle in the X-Y plane. In the Riemann fitting procedure, this circle is mapped onto the surface of a paraboloid as shown here. These points will all lie in a plane whose orientation can be used to derive the transverse momentum and ϕ angle of the track. See the text for more details about Riemann fitting.

drift times are used at this stage). The dip angle and circle parameters obtained from this step are used to resolve which side of the wires the track passed. This information is necessary to resolve the left right ambiguity and apply the correct sign to the position derived from the drift time.

At this point, care must be taken to properly fit the space points from a single package (i.e. a segment) so that the segments can be projected across the space between packages and linked together to form full candidates. For the travel time between the target and the FDC planes the particle is assumed to be a pion.

A correction is made to the space points for the Lorentz force. Due to the orientation of the magnetic field with respect to the wires, a second left-right ambiguity problem arises for the interpretation of the cathode data for the positions of the avalanches along the wire. After an ionization event in the chamber gas, the Lorentz force causes the drifting electrons to be deflected along the wire direction relative to the B=0 case. This means for the B=2.2 T case that the measured position does not correspond to the position at which the track passed through the chamber. The idea is illustrated schematically in Figure 44. The sign of this deflection depends on the direction in which the electrons are drifting in toward the wire and the magnitude of the effect depends on the position of the ionization within the drift cell. The effect can be minimized with an appropriate choice of chamber gas. Our nominal choice is 40% Argon/60% CO_2, for which the maximum deflection is about 1.6 mm. For each entry in the magnetic field map, the path of the drifting electrons for ionization points throughout a drift cell were simulated using the Garfield program[4]. An example of the deflection as a function of position is shown in Figure 45. Ignoring distortions for ionizations near the wires, the surface is well-parameterized by a plane. The effect is included in the HDGeant simulation via interpolation over a map of parameters describing these planes in a grid in r and z. Once the sign of the left-right ambiguity is resolved, the reconstruction code uses the drift distance and z-position of the hit plane to apply a correction to the hit position along the wire based on an interpolation over the same table. Once corrections for the drift distance and avalanche position are applied, the fitting procedure undergoes a "time-based" iteration which corrects the cathode information for the deflection of electrons along the wire. The circle and dip angle parameters are recomputed and the covariance matrices and the predictions for each segment's helical path are updated.

The next step is to match segments together to form track candidates. The code looks for the nearest match, propagating from one package to the next, subject to a cut of the form $\Delta r < 2.79 + 2.88/p^2$, as illustrated in Fig. 46. Once a segment has been linked into a track it is removed from the list. This means that segments cannot currently be shared between track candidates. For those segments that are linked together, the code calls the Riemann circle and line fits once more with the combined set of hits (with the exception of hits from package 4 if there are segments available from packages 1, 2, and 3). At this point the charge of the final track candidate is determined in one of two ways. First, if the charge determination for each of linked segments are in agreement, then that charge is used. Otherwise, the charge is determined from the final refit to the full set of points.

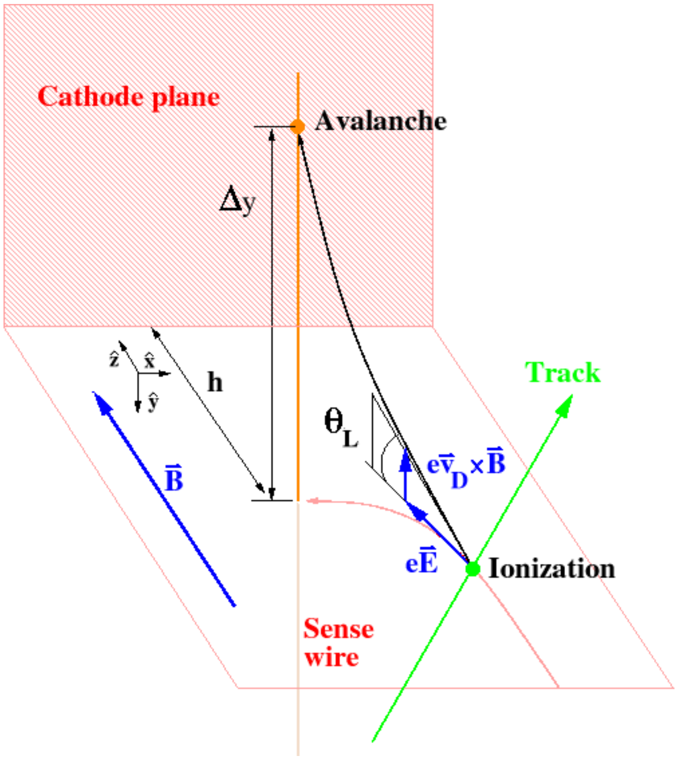

Figure 44: Diagram illustrating how the Lorentz force due to the chambers being located in a region of high magnetic field results in a shift of the avalanche position on the wire.

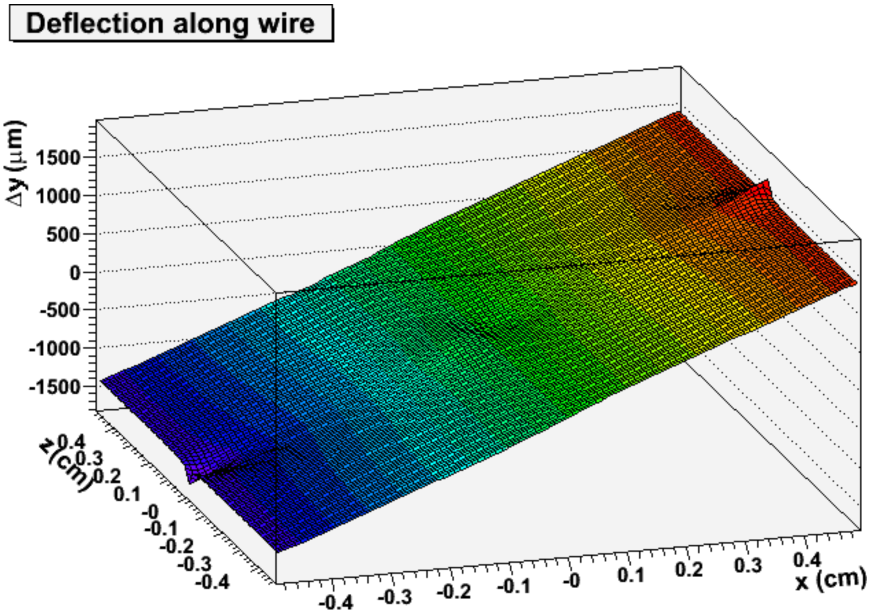

Figure 45: Example of the amount of deflection of the avalanche position as a function of the position of the ionization within a cell. For this plot the field was 2.0 T pointing along the beam axis and the gas mixture was 40% Ar/ 60% CO_2. The sense wire goes through the center of the plane.

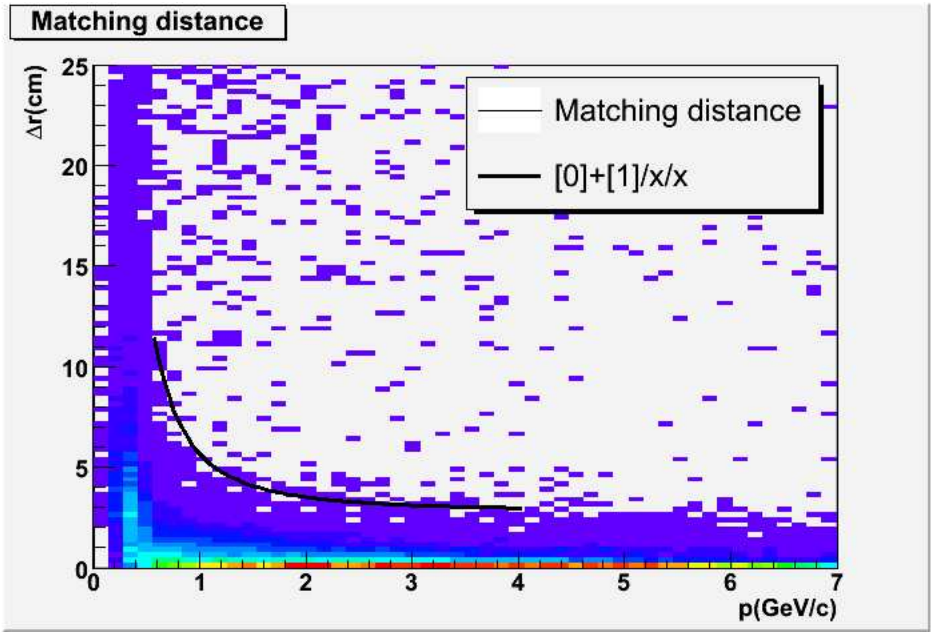

Figure 46: Difference between the projected track position and the segment to which we are matching as a function of momentum. The black curve shows the segment-matching cut.